



*“Structural Health Monitoring of civil infrastructures, using both  
GPS-Galileo HAS and accelerometric data”*

*Decreto Del Capo Dipartimento Rep. n. 2 Prot. n.35 del 13/01/2021*

## Report on the activities carried out for the European project GISCAD-OV

Università degli Studi Roma Tre

Dipartimento di Architettura

Responsabile del progetto: Dott. S. Gabriele

Assegnista di ricerca: Ing. Daniele Cinque

Roma, 10/02/2022

## Table of contents

Index of figures .....	4
Index of tables .....	8
1 Introduction.....	9
2 Background knowledge .....	12
2.1 Geodetic coordinates and geodetic datums.....	12
2.2 Geodetic coordinates transformation .....	14
3 Monitoring of a small-scale benchmark structure .....	18
3.1 Structure description .....	18
3.2 Structure modelling .....	21
3.2.1 Architectural surveying.....	21
3.2.2 FEM modelling.....	24
3.3 Monitoring system installation.....	27
3.4 Data acquisition .....	32
3.5 Data transformation .....	37
3.6 Results.....	41
3.6.1 Time domain.....	41
3.6.2 Frequency domain.....	45
3.7 Comparison with accelerometric system .....	48
3.7.1 Displacements' comparison .....	49
3.7.2 Frequencies' comparison .....	53
4 Monitoring of a full-scale benchmark structure .....	56
4.1 Structure description .....	56
4.2 Structure modelling .....	60
4.3 Monitoring system installation.....	62
4.4 Results.....	69

## Report on the activities of the European project GISCAD-OV

4.5	Comparison with accelerometric system .....	70
5	Appendix.....	74
5.1	Script for log files reading .....	74
5.2	Script for geodetic coordinates conversion.....	76
5.3	Script for data filtering.....	78
6	Bibliography.....	79

## Index of figures

Figure 1. Ellipsoid showing the ECEF-g (in blue) and the ECEF-r (in red) reference systems. .....	13
Figure 2. Ellipsoid showing ECEF-g and ECEF-r reference systems, the ellipsoidal normal through point P and the geodetic longitude of P (3). ....	13
Figure 3. Meridian plane containing point P showing the ellipsoidal normal through P, the geodetic latitude of P, the ellipsoidal height of P and both the semiminor and semimajor axis of the ellipsoid, b and a, respectively (3). ....	13
Figure 4. The geodetic ellipsoid showing the semimajor and semiminor axes (a, b), the height (h), the latitude ( $\lambda$ ) and the plumb line from the point of interest P to the z axis (1). .....	14
Figure 5. A schematic diagram for the WGS84, ECEF, and ENU coordinate systems for the Earth and their transformation relationships (PM line is the Prime Meridian; $\varphi$ and $\lambda$ are latitude and longitude in WGS84; X,Y,Z for ECEF; and E,N,U for ENU) (5).....	15
Figure 6. A schematic diagram representing the transformation of coordinates from the ENU (in red) to the local reference system (in black) where latter is referred to the tested structure (in blue). As it can be noticed, the transformation involves a rotation around the z-axis. Therefore, the z-axis of both reference systems define the normal of the ellipsoid tangent plane.....	17
Figure 7. Schematic representation of the ellipsoid showing the four coordinate systems previously considered: ECEF-g (in blue), ECEF-r (in red), ENU (in green) and local (in black). .....	17
Figure 8. Entrance of the SOGEl structure. ....	18
Figure 9. Plan view of the SOGEl structure. ....	19
Figure 10. West-South side of the SOGEl structure. ....	19
Figure 11. West-North corner of the SOGEl structure. ....	20
Figure 12. West-North side of the SOGEl structure. ....	20
Figure 13. Surveying with laser scanner technique.....	21
Figure 14. Absolute distances between point cloud. ....	22

Figure 15. First capture of point cloud. ....	22
Figure 16. Second capture of point cloud. ....	23
Figure 17. Third capture of point cloud.....	23
Figure 18. Fourth capture of point cloud. ....	23
Figure 19. Fifth capture of point cloud.....	24
Figure 20. Geometrical model in AutoCAD. ....	25
Figure 21. Schematic plan view of the structure, being the position of the antennas highlighted.....	25
Figure 22. Standard view of the structural model in SAP2000. ....	25
Figure 23. Extrude view of the structural model in SAP2000. ....	26
Figure 24. View of the first mode shape of the structure in SAP2000.....	26
Figure 25. Installation of the NovAtel antenna and the accelerometer. ....	28
Figure 26. Topographic leveling base used in the installation of the antennas.....	28
Figure 27. On-field sketch of a plan view of the north section of the benchmark structure showing the location of the NovAtel instrumentation and the accelerometers. ....	29
Figure 28. Test configuration.....	29
Figure 29. First view of the GNSS system configuration. ....	30
Figure 30. Second view of the GNSS system configuration.....	30
Figure 31. Third view of the GNSS system configuration. ....	31
Figure 32. Fourth view of the GNSS system configuration. ....	31
Figure 33. Dynamic test.....	32
Figure 34. Conversion from BINARY to ASCII using NovAtel Converter2.6.7.....	33
Figure 35. Message structure of the ASCII file (7).....	33
Figure 36. Example of ASCII message where the three main fields have been highlighted (header in red, data in black and end in blue). ....	34
Figure 37. Example of ASCII message header structure taken from Figure 26. ....	34
Figure 38. Example of ASCII message data structure taken from Figure 25. ....	35
Figure 39. Position of the NovAtel antennas in ECEF-r reference system. ....	38
Figure 40. Position of the NovAtel antennas in ENU reference system.....	38
Figure 41. Position of the NovAtel antennas in EN reference system. ....	38

Figure 42. Position of NovAtel antennas in local reference system. ....	39
Figure 43. Position of the first antenna during the first test in geodetic coordinates.....	40
Figure 44. Displacements of the first antenna during the first test in local coordinates. ..	40
Figure 45. Filtered displacements of the first antenna during the first test in local coordinates.....	41
Figure 46. Displacements along the three local axes of the antenna 1. ....	42
Figure 47. Displacements along the three local axes of the antenna 2. ....	43
Figure 48. Displacements along the three local axes of the antenna 3. ....	43
Figure 49. Displacements along the three local axes of the antenna 4. ....	44
Figure 50. Displacements along the three local axes of the antenna 5. ....	44
Figure 51. Signal range (highlighted in green) of the NovAtel signal containing information about the free oscillations of the system. ....	46
Figure 52. PSD of range 1. ....	47
Figure 53. PSD of range 2. ....	47
Figure 54. Comparison between the NovAtel and the accelerometric data. ....	49
Figure 55. Comparison between the first antenna and accelerometer.....	50
Figure 56. Comparison between the second antenna and accelerometer.....	50
Figure 57. Comparison between the third antenna and accelerometer. ....	51
Figure 58. Comparison between the fourth antenna and accelerometer. ....	51
Figure 59. Comparison between the fifth antenna and accelerometer. ....	51
Figure 60. Signal range (highlighted in green) of the NovAtel and the accelerometric system containing information about the free oscillations of the system.....	53
Figure 61. Comparison between the PSD of the NovAtel and accelerometric signals, considering the free oscillations due to the first excitation. ....	54
Figure 62. Comparison between the PSD of the NovAtel and accelerometric signal, considering the free oscillations due to the second excitation. ....	54
Figure 63. Static system of the bridge road. ....	56
Figure 64. Drone view of the road bridge. ....	57
Figure 65. Drone view of the second span of the bridge. ....	57
Figure 66. View of the road from on top of the deck.....	58

Figure 67. View from below the deck of the four box girders and the two piers that supports the second span.....	58
Figure 68. Details of the four box girders.....	59
Figure 69. Details of the pier. ....	59
Figure 70. Cloud point, shade of grey view of the second span. ....	60
Figure 71. Cloud point, reflected light intensity view of the second span.....	61
Figure 72. Cloud point, reflected light intensity view of the road. ....	61
Figure 73. Cloud point, reflected light intensity view of the monitored point. ....	62
Figure 74. First view of the worksite. ....	63
Figure 75. Second view of the worksite. ....	63
Figure 76. Third view of the worksite.....	64
Figure 77. Antenna installed on guardrail. ....	64
Figure 78. Antenna and accelerometer installed on the guardrail in order to monitor the same point.....	65
Figure 79. Accelerometer mount on the top part of the guardrail.....	65
Figure 80. Accelerometer mount on the bottom part of the guardrail. ....	66
Figure 81. Schematic representation of the plan view of the bridge, being the position of the three antennas highlighted.....	67
Figure 82. View of the antennas installed in the first (in foreground) and the second monitored point (in background).....	67
Figure 83. View of the antennas installed in the first (in background) and the second monitored point (in foreground).....	68
Figure 84. View of the antenna installed in the third monitored point.....	68
Figure 85. Position of the antenna 2 in geodetic coordinates. ....	69
Figure 86. Vertical displacements of antenna 1 in local coordinates. ....	70
Figure 87. Comparison of the displacements acquired by the accelerometric and the G-HAS system.....	71
Figure 88. Comparison of the peak displacement.....	72
Figure 89. Comparison of the peak displacements of all the sensors mounted on the bridge. ....	73

## Index of tables

Table 1. ASCII message header structure (7).....	35
Table 2. ASCII message data structure (7).....	36
Table 3. Peaks of displacements.....	45
Table 4. Peak frequencies.....	46
Table 5. Mean peak frequencies. ....	47
Table 6. Comparison between the NovAtel signal and the FEM model in the frequency domain.....	48
Table 7. Peaks of displacements acquired by the two monitoring systems. ....	52
Table 8. Differences between the two monitoring systems in terms of peaks of displacements.....	52
Table 9. Mean difference of peaks of displacements between the two monitoring systems. ....	52
Table 10. Peak frequencies of the NovAtel and accelerometric system.....	55
Table 11. Differences of the peak frequencies between the NovAtel and the accelerometric system.....	55
Table 12. Mean difference of the peak frequencies. ....	55



## 1 Introduction

The present report refers to the work carried out by the University Roma Tre (UNIROMA3) for the European project GISCAD-OV (Galileo Improved Services for Cadastral Augmentation Development On-field Validation) co-funded by the Horizon 2020 programme of the European Union. The main objective of the project is to design, develop and validate an innovative and cost-effective High Accuracy Service (HAS) for Cadastral Surveying applications, based on GPS+Galileo HAS and Precise Point Positioning-Ambiguity Resolution (PPP-AR) quick convergence techniques. The great advantage of the GPS+Galileo HAS services is that it will be useful in case of unavailability of terrestrial communication links, hence, in case of disaster management situations, such as floods or earthquakes, as well as for a continuous monitoring in case of infrastructure monitoring applications. Currently, the most used seismic monitoring systems are the accelerometers, which are based on the measure of accelerations. From the measured accelerations, one can obtain the displacements by double integration in the time-domain and furthermore, the frequency content of the acceleration or displacement spectra. Both the displacements and the frequency content can be used as parameters to assess the integrity of the monitored structure. However, the post-processing of the measured accelerations suffer for numerical errors due to the limitation induced by experimental noise and the sampling frequency. A direct measurement of the relative displacements during a seismic event carried out through GPS+Galileo HAS could be very useful firstly, to improve the double integration conditioning. This will also allow reducing the number of accelerometers attached to the structure and the cost of monitoring systems. Current state of the art and applications show that it is possible to implement a GNSS (Global Navigation Satellite System) based monitoring system (exploiting also advanced PPP technologies), with sampling frequency up to 50Hz. For civil structures and infrastructures, the frequency range of interest in seismic applications is limited between 0.1 Hz and 15 Hz. The frequencies of the main modes of vibration are usually below 4 Hz. This means that the frequency range of interest is ideally fully covered. Therefore, the GISCAD-OV project is also devoted to study new low-cost monitoring systems without using a large number of expensive

accelerometers. For seismic surveying and monitoring, the direct measure of relative displacements and inter-floor drifts would be the main parameter for predicting the state of the structure, before and after an earthquake. Furthermore, terrestrial systems are distinct in measuring static and dynamic displacements. The new proposed technology allows measuring both kinds of displacements. The GPS+Galileo HAS will be a cost-effective solution for monitoring structures that are not endowed with a terrestrial monitoring system.

The work described in the present work was developed during the 12-month period that goes from March 2021 to March 2022 and is ongoing. The work is framed in the activities of Work Package 4 (WP4), Pilot Project, and Work Package 5 (WP5), Validation, of the GISCAD-OV project. UNIROMA3 is the task leader of Tasks 4.3 (T4.3) and 5.6 (T5.6). Both tasks are devoted to the topic “Infrastructure monitoring and 3D surveying”. The main objective of the tasks is to analyse the efficiency and the accuracy of the GNSS based structural monitoring system (exploiting advanced PPP technologies), with sampling frequency up to 50 Hz, and to show whether or not the system can be applied in the monitoring of civil infrastructures. The system being analysed is based on the integration of GPS+Galileo HAS. The efficiency and accuracy of the system were tested during T4.3 on a small-scale benchmark structure through a comparative analysis based on the results obtained by an accelerometric monitoring system, installed by the Italian Department of Civil Protection (DPC), and a Finite Element Model (FEM) of the structure, implemented by UNIROMA3. The latter was implemented thanks to a 3D survey conducted on the structure by means of a laser scan. The comparative analysis is in both the frequency and time domain. Hence, the main goal of T4.3 was to obtain the principal vibration frequencies of the tested structure from the GPS+Galileo HAS system, the accelerometric system and the FEM model and to obtain the estimation of the maximum amplitude displacements, that could be further used as indicators for structural safety, from both the monitoring systems. The methodology adopted in T4.3 was then applied to T5.6, which is still ongoing. This task is devoted to the validation of the Pilot Project’s results. For this purpose, the GNSS system was tested on a full-scale benchmark structure through a comparative analysis based on the results obtained by the same accelerometric system already used in T4.3. The results

acquired by the two monitoring system were compared in the time domain by means of the displacements acquired. The knowledge to post process the satellite signal is crucial in order to achieve the goal of the task. Indeed, the GPS+Galileo HAS system and the accelerometric system acquire data in the geodetic and the local reference system, respectively. Therefore, it is mandatory to be able to convert the data acquired from the GPS+Galileo HAS system in order to proceed with the comparative analysis.

The text is divided in a first introductory section in which the basic knowledge for a full comprehension of the text is explained. Moreover, the equations of the coordinates' conversion method are displayed. Following this brief introduction the application of the conversion method to real data is shown. In particular, chapter 3 is devoted to the work developed as Pilot Project, in which the GNSS system is tested on a small-scale benchmark structure. Chapter 4, instead, is devoted to the validation process, in which the GNSS system is tested on a full-scale benchmark structure. As a reminder, T4.3 and T5.6 are still ongoing. Therefore, the results that will be further illustrated must be considered as preliminary results.

## 2 Background knowledge

### 2.1 Geodetic coordinates and geodetic datums

The position acquired by the satellite system is in geodetic coordinates which are calculated in the Earth Centred-Earth Fixed geodetic (ECEF-g) reference system, the customary reference for the GNSS (1). The coordinates for this frame are the geodetic latitude, longitude and height. The first two, which are referred to as  $\phi$  and  $\lambda$ , respectively, are angular distances that specify the horizontal position of the point of interest on the surface of the earth. The third one, which is referred to as  $h$ , is the elevation of the point of interest above the surface of the earth. Therefore, geodetic coordinates are defined relatively to a particular Earth geodetic datum, which is a means of representing the figure of the Earth (2). The geodetic datum is usually an oblate ellipsoid of revolution that approximates the surface of the Earth, being characterized by a semimajor and semiminor axis. The ellipsoid can be easily obtained considering a Cartesian reference system. The revolution of the ellipsoid is about the polar axis  $Z$  while the axes  $X$  and  $Y$  are positioned in order that the positive  $X$ -axis defines zero longitude while the positive  $Y$ -axis is chosen to complete an orthogonal right-handed coordinate system (3). This Cartesian reference system with origin  $O$  in the centre of the ellipsoid is usually referred to as Earth Centred-Earth Fixed rectangular (ECEF-r) reference system. Once the geodetic datum is specified, the geodetic coordinates can be defined relatively to the ECEF-g reference system. Latitude  $\phi$  is defined as the angle between the ellipsoidal normal through the point of interest and the equatorial plane. Longitude  $\lambda$  is defined as the angle between the meridian that contains the point of interest and the Prime meridian, also known as Greenwich meridian. Finally, height  $h$  is defined as the elevation of the point of interest above the surface of the ellipsoid. Since the geodetic coordinates are measured relative to a fixed point on the surface of the earth, ECEF-g rotates at the earth rate, i.e. it is a non-inertial frame.

Figure 1 displays both the reference systems introduced so far. Figure 2 and Figure 3 show how to calculate the geodetic coordinates. Since the geodetic datum is an ellipsoid, the ellipsoidal normal through point  $P$  does not cross the origin of the reference system unlike what happens when a sphere is considered.

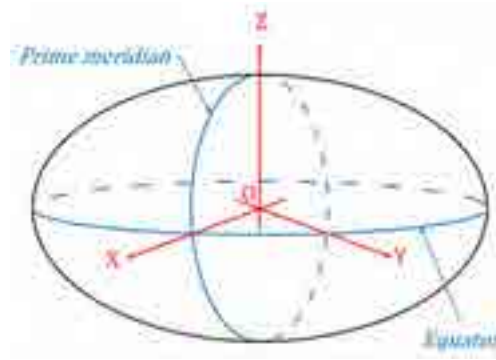


Figure 1. Ellipsoid showing the ECEF-g (in blue) and the ECEF-r (in red) reference systems.

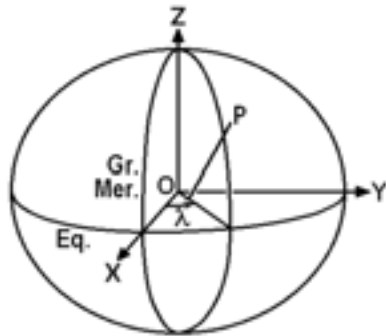


Figure 2. Ellipsoid showing ECEF-g and ECEF-r reference systems, the ellipsoidal normal through point P and the geodetic longitude of P (3).

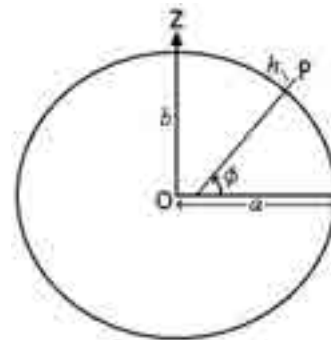


Figure 3. Meridian plane containing point P showing the ellipsoidal normal through P, the geodetic latitude of P, the ellipsoidal height of P and both the semiminor and semimajor axis of the ellipsoid, b and a, respectively (3).

Since the geodetic coordinates are dependent on the geodetic datum, they will differ between datums. The geodetic datum that is adopted in the present work is known as WGS84 (World Geodetic System 1984) and it is geometrically defined as follows:

*Semimajor axis*  $a = 6378137.000000 \text{ m}$

*Semiminor axis*  $b = 6356752.314245 \text{ m}$

*Flatness*  $f = \frac{a - b}{a} = 3.3528107 \times 10^{-3}$

*Eccentricity*  $e = \sqrt{f(2 - f)} = 8.1818191$

*Normal radius of curvature*  $N(\phi) = \frac{a}{\sqrt{1 - e^2 \sin^2(\phi)}}$

Figure 4 displays the meridian plane of the ellipsoid that contains the point of interest P together with the geometrical features of the ellipsoid. In particular, the normal radius of curvature  $N$  is graphically defined as the distance along the ellipsoid normal between the vertical projection of P on the ellipsoid surface and the semiminor axis  $b$ .

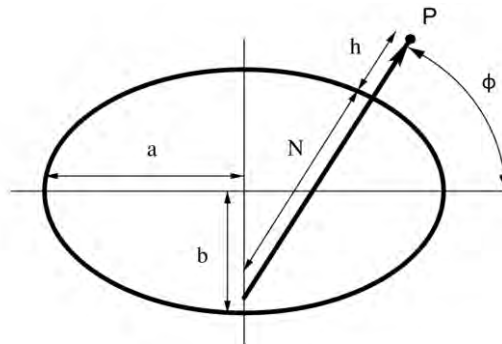


Figure 4. The geodetic ellipsoid showing the semimajor and semiminor axes ( $a$ ,  $b$ ), the height ( $h$ ), the latitude ( $\lambda$ ) and the plumb line from the point of interest P to the z axis (1).

## 2.2 Geodetic coordinates transformation

The data acquired by the GNSS system is organized in WGS84 geodetic coordinate system. On the other hand, the accelerometers' signal is organized in its local coordinate system, which means that the coordinate system depends on the position chosen for the accelerometer during the installation process. Since the displacements of the tested structure that we were interested in were the out-of-plane displacements, the accelerometers were installed accordingly to the local reference system of the structure. Therefore, the local coordinate system refers to the tested structure. In order to be able to compare the two set of data, one needs to express the signals of both the GNSS and the accelerometric system in a common coordinate system. This is why there is the necessity to apply coordinate transformation equations. For this purpose, it has been decided to consider the local coordinate system of the tested structure as reference. Hence, the accelerometers signal do not need to be transformed unlike the satellite signal. The straightforward method to convert the geodetic coordinates to local coordinates involves three different coordinate transformations. The first one involves a coordinate conversion from the ECEF-g to the ECEF-r reference system. Equations [1(1, 3)] that are explained in the work by Heiskanen and Moritz (4), allow this transformation.

$$X = (h + N) \cos \phi \cos \lambda \quad (1)$$

$$Y = (h + N) \cos \phi \sin \lambda \quad (2)$$

$$Z = (h + (1 - e^2)N) \sin \phi \quad (3)$$

Once the coordinates are in the ECEF-r frame, there is the necessity to apply a second transformation in order to obtain a tangent plane coordinate system, known as East-North-Up reference system (ENU). It is still a Cartesian system but the first two coordinates' axes are in the plane tangent to the surface of the ellipsoid. Therefore, these two axes define the ellipsoid tangent plane rather than the equatorial plane as in the ECEF-r reference system. The origin  $O'$  is a reference point in the region of interest. This may be on the ellipsoidal surface, or above or below it. The axis  $Z'$  is the ellipsoidal normal through  $O'$ , so it is approximately the local vertical. The plane that contains the axes  $X'$  and  $Y'$  is perpendicular to the  $Z'$ -axis, so it is approximately horizontal in the area. The three axes  $X'$ ,  $Y'$  and  $Z'$  identify an orthogonal right-handed coordinate system and they point towards east, north and up respectively. This is why, for this work it was decided to adopt the nomenclature of E, N and U for the  $X'$ ,  $Y'$  and  $Z'$  respectively. The three different coordinate systems are shown in Figure 5.

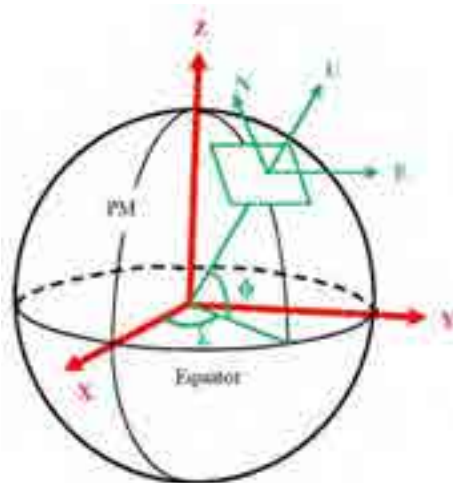


Figure 5. A schematic diagram for the WGS84, ECEF, and ENU coordinate systems for the Earth and their transformation relationships (PM line is the Prime Meridian;  $\phi$  and  $\lambda$  are latitude and longitude in WGS84;  $X, Y, Z$  for ECEF; and  $E, N, U$  for ENU) (5).

The great advantage of the ENU system is that its axes coincide with the expectation of people on the ground concerning such ingrained things as up, and north, which something like ECEF-r does not (1). The transformation from ECEF-r to ENU can be built up from a sequence of simple translation and rotations, resulting in an orthogonal transformation matrix shown in Equation (4), explained in the work Heiskanen and Moritz (4).(4)(4)

$$\begin{pmatrix} E \\ N \\ U \end{pmatrix} = \begin{pmatrix} -\sin(\lambda) & \cos(\lambda) & 0 \\ -\cos(\lambda)\sin(\phi) & -\sin(\lambda)\sin(\phi) & \cos(\phi) \\ \cos(\phi)\cos(\lambda) & \cos(\phi)\sin(\lambda) & \sin(\phi) \end{pmatrix} \begin{pmatrix} X - X_0 \\ Y - Y_0 \\ Z - Z_0 \end{pmatrix} \quad (4)$$

In the above equation,  $X_0$ ,  $Y_0$  and  $Z_0$  are the coordinates of the origin  $O'$  of the ENU coordinate system expressed in the ECEF-r coordinate system.

Lastly, the data must be organized in the local reference system of the tested structure according to the disposition of the accelerometers. In the present work, the tested structure lay on the ellipsoid tangent plane as shown in Figure 6. Hence, the coordinate transformation involves a 2D rotation about the z-axis, which represents the normal of the ellipsoid tangent plane. The transformation matrix that is used for a clockwise rotation  $\alpha$  is shown in Equation (5).

$$\begin{pmatrix} X_L \\ Y_L \\ Z_L \end{pmatrix} = \begin{pmatrix} \cos(\alpha) & -\sin(\alpha) & 0 \\ \sin(\alpha) & \cos(\alpha) & 0 \\ 0 & 0 & 1 \end{pmatrix} \begin{pmatrix} E \\ N \\ U \end{pmatrix} \quad (5)$$



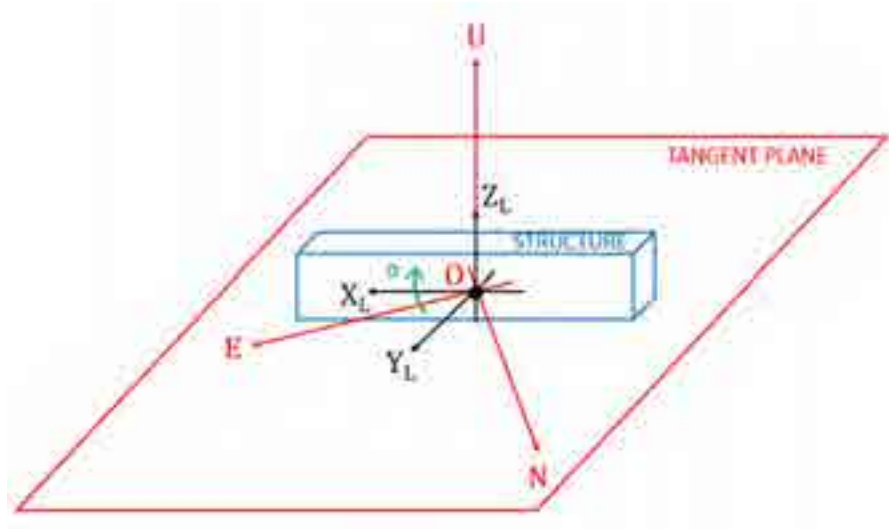


Figure 6. A schematic diagram representing the transformation of coordinates from the ENU (in red) to the local reference system (in black) where latter is referred to the tested structure (in blue). As it can be noticed, the transformation involves a rotation around the z-axis. Therefore, the z-axis of both reference systems define the normal of the ellipsoid tangent plane.

In conclusion, the straightforward method to convert the geodetic coordinates to local coordinates implies a three-step transformation process: a first conversion in ECEF-r, a second in ENU and the last in the local reference system. The four different coordinate systems that were considered in the previous discussion are shown in Figure 7.

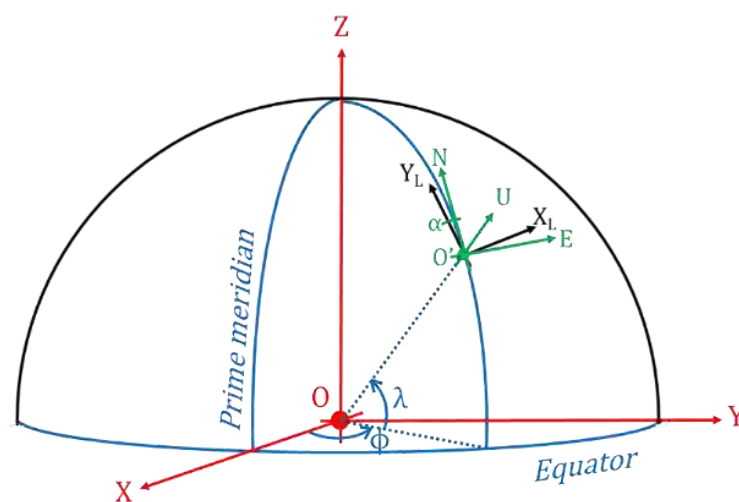


Figure 7. Schematic representation of the ellipsoid showing the four coordinate systems previously considered: ECEF-g (in blue), ECEF-r (in red), ENU (in green) and local (in black).

### 3 Monitoring of a small-scale benchmark structure

#### 3.1 Structure description

A flexible steel structure has been chosen as a small-scale benchmark for developing the activities of the Pilot Project within T4.3. This structure is located on the top roof of one of SOGEI's buildings in Rome. The structure is composed of a steel frame, panelled with a steel grillage, as depicted in Figures [8, 12].



*Figure 8. Entrance of the SOGEI structure.*



Figure 9. Plan view of the SOGEI structure.



Figure 10. West-South side of the SOGEI structure.



*Figure 11. West-North corner of the SOGEI structure.*



*Figure 12. West-North side of the SOGEI structure.*

## 3.2 Structure modelling

### 3.2.1 Architectural surveying

The benchmark structure has been surveyed to realize a 3D FEM model. A 3D survey, based on remote sensing technology, was performed with laser scanner technique (Figure 13) producing more than 71 million points, and 9 aligned point clouds. For decades, remote sensing technology has been used in the field of surveying and for this purpose, a ZF 5010x Laser Scanner was adopted and each point cloud was aligned with the Z+F LaserControl® Scout software. The goal of this kind of survey was to realize an accurate 3D FEM model by minimizing errors in the measure of the structural parts. The entire alignment has been refined and verified to produce fine aligned clouds. The alignment process resulted in more than 75% of points having less than 6 mm error (Figure 14). In order to realize the FEM model, cross sections have been extracted from the point cloud (Figures [15, 19]) using a procedure described by Canciani (6). Therefore, the centres of gravity of the steel elements, the pillars and the beams were calculated. Those features were then used to build a geometrical model in AutoCAD that served as a baseline for the implementation of the structural model.



*Figure 13. Surveying with laser scanner technique.*

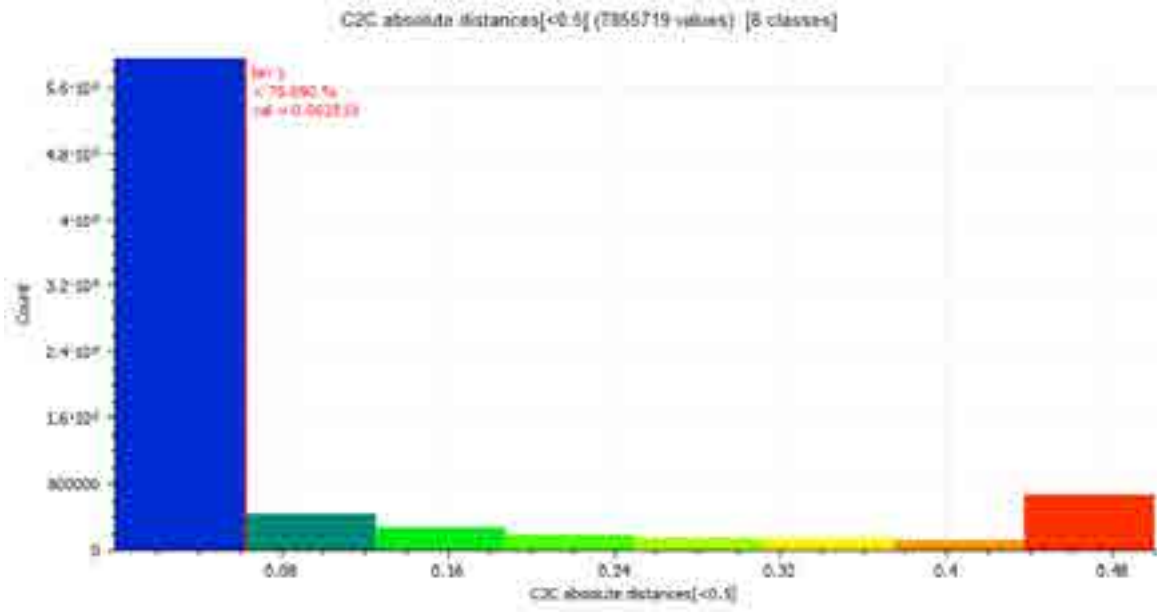


Figure 14. Absolute distances between point cloud.

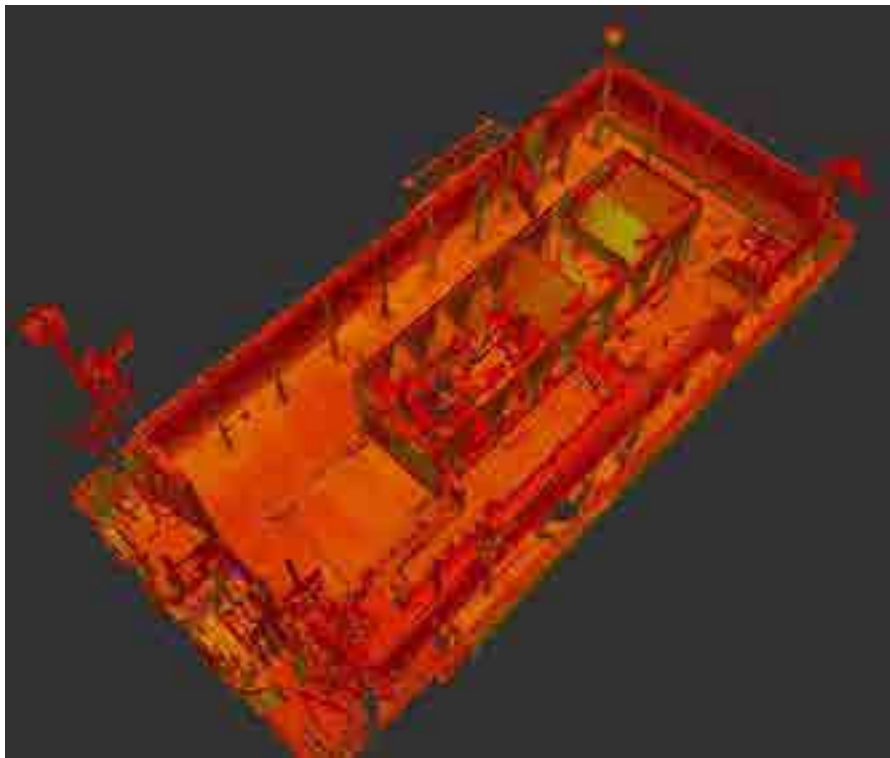
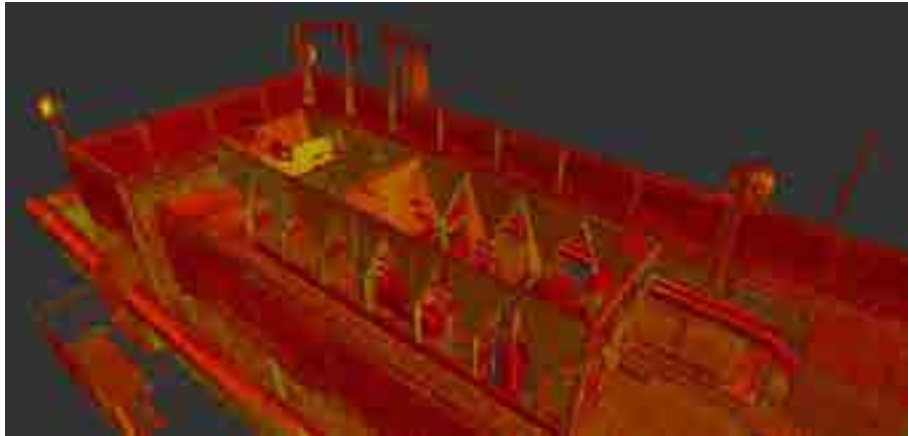
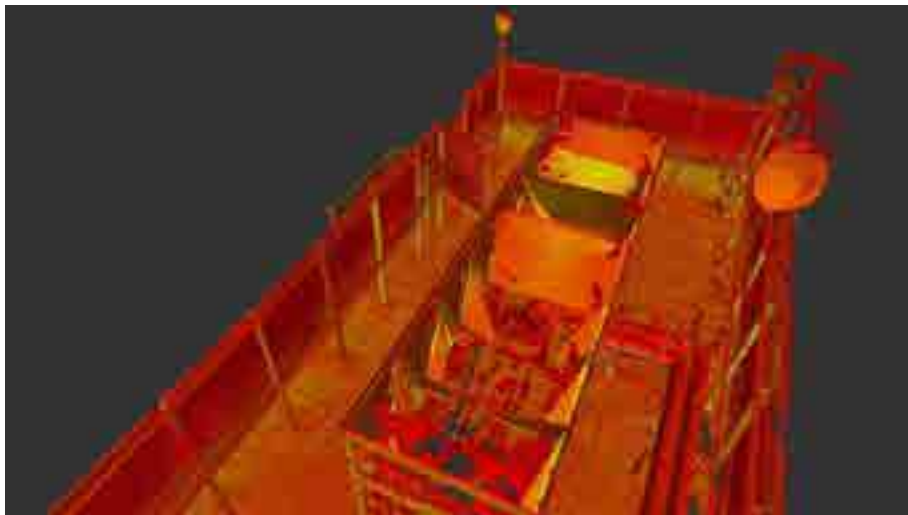


Figure 15. First capture of point cloud.



*Figure 16. Second capture of point cloud.*



*Figure 17. Third capture of point cloud.*

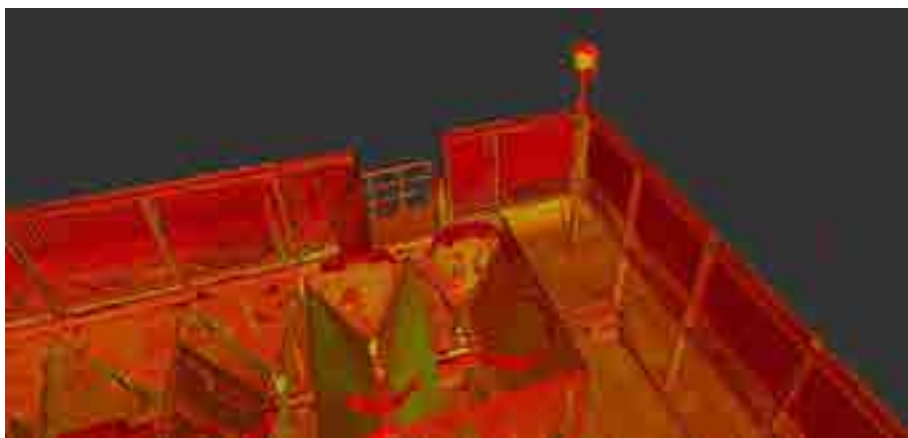


*Figure 18. Fourth capture of point cloud.*

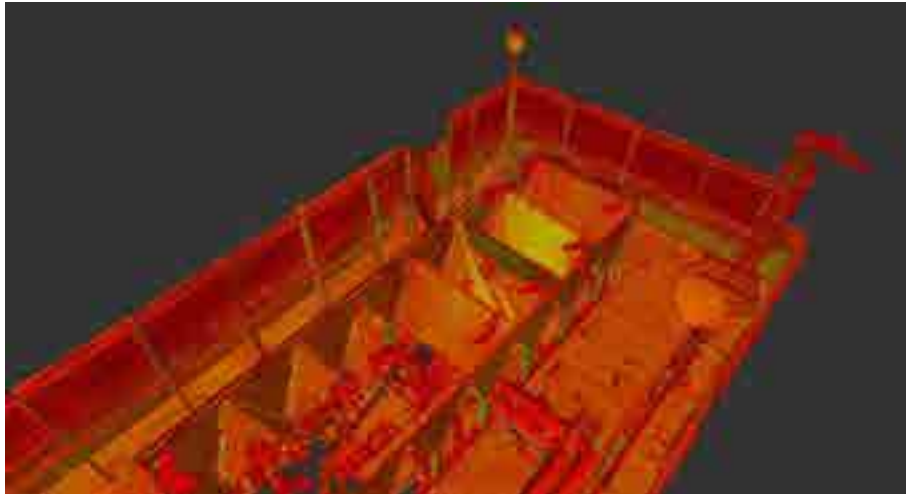


*Figure 19. Fifth capture of point cloud.*

### 3.2.2 FEM modelling

Once the architectural surveying was completed and the cloud of points was successfully acquired a geometrical model of the structure was created in AutoCAD (Figure 20). This served as a baseline for the implementation of the structural model. Indeed, the geometrical model was obtained directly from the cloud of points by calculating the gravity centre of each cross section and then drawing the axis of each structural element through this point. Hence, the model is represented by a one dimensional element frame.

The geometrical model was then imported in SAP2000 in order to create the structural model. Since the antennas being tested were installed only on part of the structure (Figure 21), it was decided to implement a model that could describe the dynamic behaviour of this portion of structure. The model depicted in Figure 22 and Figure 23 shows the portion of structure that was considered for the installation of the antennas. The remaining part of structure was taken into consideration through a system of suitably designed external constraints that could correctly describe the dynamic behaviour of the entire structure. All the structural elements that create the steel frame are considered as beam elements. The cross section of each structural element was assigned through SAP2000. Since the axes of the structural elements do not always intersect, a series of body constraints were necessary in order to recreate the continuity in the structure.



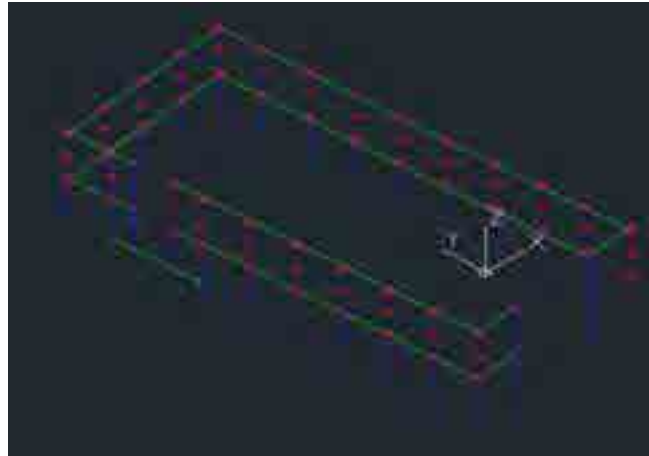


Figure 20. Geometrical model in AutoCAD.

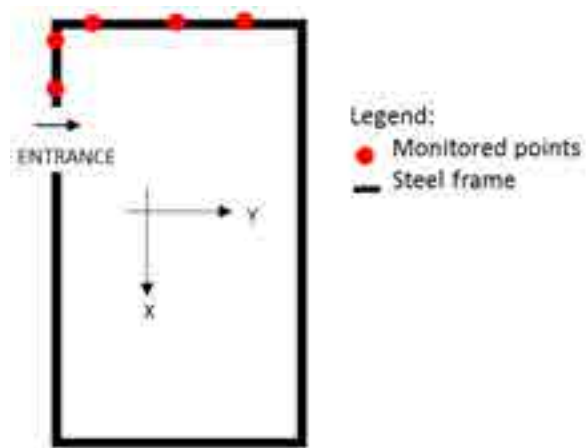


Figure 21. Schematic plan view of the structure, being the position of the antennas highlighted.

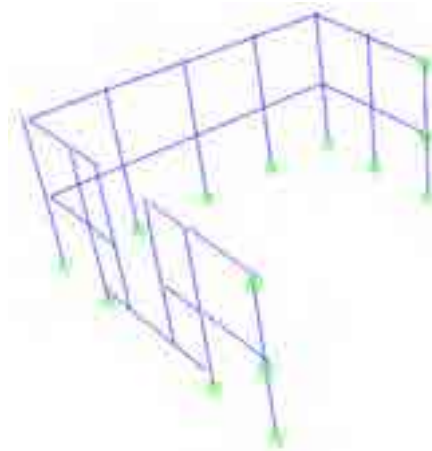


Figure 22. Standard view of the structural model in SAP2000.



Figure 23. Extrude view of the structural model in SAP2000.

The model was used to evaluate the natural frequency of the structure. Figure 24 shows the first mode shape of the structure, in which it can be noticed how the upper parts of the structure, on which the antennas were installed, are the parts that are subjected to the highest displacements. The frequency of the first vibrational mode is 5.11 Hz. The calibration of the FEM model with the data collected by the accelerometers is ongoing.

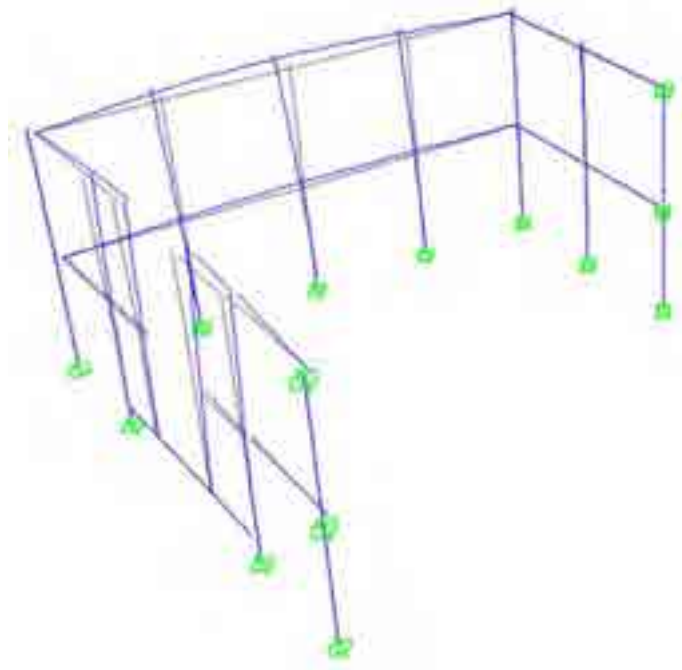


Figure 24. View of the first mode shape of the structure in SAP2000.

### 3.3 Monitoring system installation

In order to test the GNSS system, the small-scale benchmark structure, object of T4.3, was also monitored with the accelerometers. A set of five piezoelectric single axis accelerometers were employed, that is, PCB 393A03 by Piezotronics, which are Voltage Mode output sensors characterized by an high sensibility level, 1000 mV/g, and a measurement range equal to  $\pm 5g$  with a frequency range from 0.5 to 2000 Hz with a 5% of errors. Each accelerometer was connected to a 24-channels data logger, that is, LMS-SCADAS mobile hardware with 24-bit A/D for a dynamic range of 150 dB, by shielded cables of 3, 6, or 10 m. The accelerometers were installed by the DPC closely to the five antennas of the GNSS system. This configuration allows acquiring the displacements of the same points of the structure with both the monitoring systems. Figure 25 shows an example of the configuration.

The GNSS system was provided by the Canadian company NovAtel Inc. It consisted of an antenna able to capture radio signals from the European navigation satellite, Galileo. A receiver, linked to the antenna, allows acquiring the signal exploiting PPP technologies. The generic NovAtel antenna has been fixed to a topographic levelling base to reach an optimal levelling. Both have been fixed with a g-clamp to the benchmark structure. The installation system is shown in Figure 26. Figure 27 shows a schematic plan view of the portion of benchmark structure on which the monitoring systems were mounted. Numbers from 1 to 5 represent the location of both the antennas and the accelerometers. The green arrow represent the directions of the excitation performed on the structure during the test. Figure 28 shows the test configuration, being both the number of the location of the monitoring systems and the local reference system highlighted. Figures [29, 32] illustrate a photo gallery of the satellite system configuration.

The test consisted of four time series acquisitions. The first one without excitation, in order to define the displacements baseline and to characterize the noise associated to the satellite signal. The other acquisitions were performed under manual excitation in order to study the correspondence between the two monitoring systems. Therefore, two types of excitations were manually impressed on the structure: the first one along the y-axis (Figure 33) while the second one along the x-axis. The first type of excitation was performed during

the second and the fourth test while the second type during the third test. Throughout the test, the excitation was performed twice. The test was conducted by means of an only output method, which means only the output was acquired since we were not interested in the input.



Figure 25. Installation of the NovAtel antenna and the accelerometer.



Figure 26. Topographic leveling base used in the installation of the antennas.

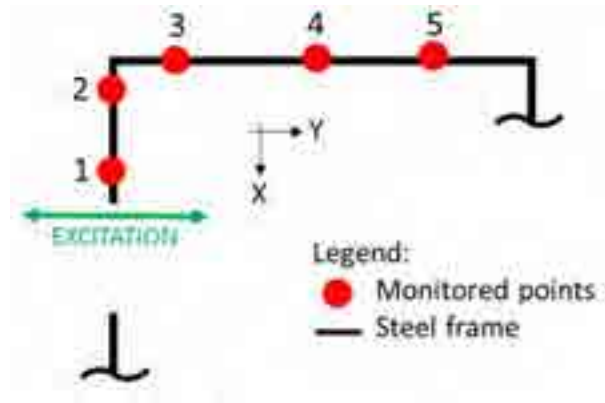


Figure 27. On-field sketch of a plan view of the north section of the benchmark structure showing the location of the NovAtel instrumentation and the accelerometers.



Figure 28. Test configuration.



*Figure 29. First view of the GNSS system configuration.*



*Figure 30. Second view of the GNSS system configuration.*



*Figure 31. Third view of the GNSS system configuration.*



*Figure 32. Fourth view of the GNSS system configuration.*



*Figure 33. Dynamic test.*

### 3.4 Data acquisition

The log files generated by the NovAtel receivers contain data in binary format. This means that before being able to extrapolate the measurements of the displacements, data must be converted by using an appropriate converter tool. In this case, the NovAtel converter version 2.6.7 provided by the company was used, as shown in Figure 34. The conversion was made from binary to ASCII format.



## Report on the activities of the European project GISCAD-OV

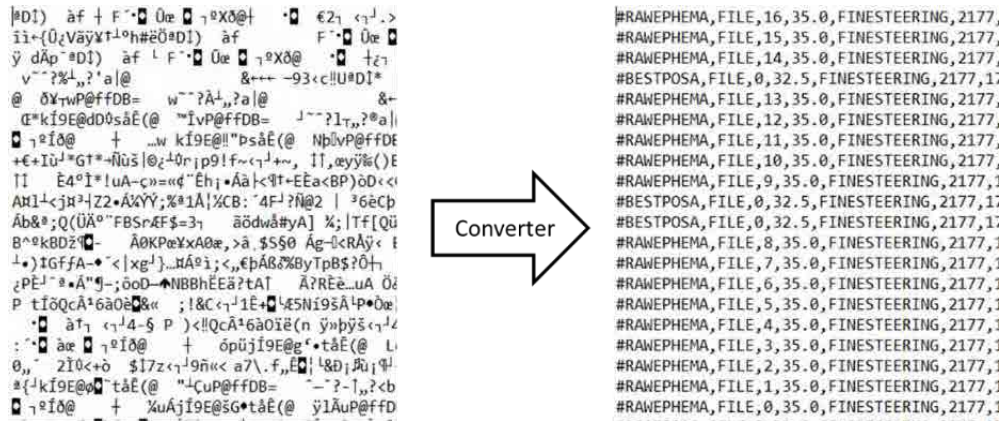


Figure 34. Conversion from BINARY to ASCII using NovAtel Converter2.6.7.

Once the data is converted, it is necessary to extrapolate the measurements of the displacements. Hence, the Commands and Logs Reference Manual (7) by NovAtel was consulted in order to write a MATLAB script that extrapolates the measurements from the converted ASCII file. The script that can be found in the appendix is based on the knowledge of the content of the ASCII file. As reported by the manual (7), the structures of all ASCII messages follow the general conventions as noted here:

1. The lead code identifier for each record is '#';
2. All data fields are delimited by a comma ',' with two exceptions:
  - The first exception is the last header field which is followed by a ';' to denote the start of the data message;
  - The second exception is the last data field, which is followed by a '\*' to indicate end of message data;
3. Each log ends with a hexadecimal number preceded by an asterisk and followed by a line termination using the carriage return and line feed characters.

As depicted in Figure 35 and Figure 36, all ASCII messages structure consist of a header, a data field and a tail indicating the end of the message.



Figure 35. Message structure of the ASCII file (7).

```
#BESTPOSA,FILE,0,26.5,FINESTEERING,2176,462388.100,02000800,cdba,16624;SOL_COMPUTED,NARROW_INT,42.45157584163,12.39625916110,64.1749,49.1000,WGS84,0.0072,0.0065,0.0168,"0",1.100,0.000,41,37,37,36,00,21,f,37"25e9ca10
```

Figure 36. Example of ASCII message where the three main fields have been highlighted (header in red, data in black and end in blue).

The importance of the header field is that contains first the indication about the type of message and second about the GPS time. Since we are interested in the extrapolation of the measured displacements, we focused on the BESTPOS type, which stands for best position. This log contains the best position computed by the receiver. The ASCII message header structure, of which an example is displayed in Figure 37, is described in Table 1. As it can be seen from the table below, the seventh and the eight header fields give information about the GPS time. More precisely, the seventh header field indicate the GPS reference week number. In the 1970s, when the GPS system was originally designed, 10 bits were assigned to the week number in the navigation data. As a result, the transmitted week number can have a value from 0 to 1023 ( $= 2^{10} - 1$ ). After the maximum value is reached, the week number “rolls over” to 0 and starts counting again. Therefore, the transmitted week number jumps back to zero every 1024 weeks (about 20 years) (8). As reported in the manual by NovAtel (7), the GPS reference week number provided in the raw satellite data is the 10 least significant bits (or 8 least significant bits in the case of the almanac data) of the full week number. When the receiver processes the satellite data, the week number is decoded in the context of the current era and therefore is computed as the full week number starting from week 0 or January 6, 1980. Therefore, in all log headers and decoded week number fields, the full week number is given. On the other hand, the eight header field contains the seconds from the beginning of the GPS reference week. Indeed, the GPS satellites transmit the time in two parts: the week number and the elapsed number of seconds within that week. Hence, besides extrapolating the displacements measurements from the data field, we made sure to extrapolate the time information from the header field in order to associate the displacement measurements to a time domain.

```
#BESTPOSA,FILE,0,26.5,FINESTEERING,2176,462388.100,02000800,cdba,16624; ...
```

Figure 37. Example of ASCII message header structure taken from Figure 36.

## Report on the activities of the European project GISCAD-OV

Table 1. ASCII message header structure (7).

Field	Field Name	Field Type	Description	Ignored on Input
1	Sync	Char	Sync character. The ASCII message is always preceded by a single '#' symbol	N
2	Message	Char[]	The ASCII name of the log or command	N
3	Port	Char[]	The name of the port from which the log was generated. The string is made up of the port name followed by an '_x' where x is a number from 1 to 31 denoting the virtual address of the port. If no virtual address is indicated, it is assumed to be address 0	Y
4	Sequence #	Long	Used for multiple related logs. It is a number that counts down from N-1 to 0, where 0 means it is the last one of the set. Most logs only come out one at a time in which case this number is 0	N
5	% Idle Time	Float	The minimum percentage of time the processor is idle, calculated once per second	Y
6	Time Status	Enum	The value indicates the quality of the GPS reference time (see Table 11: GPS Reference Time Status on page 48)	Y
7	Week	Ulong	GPS reference week number	Y
8	Seconds	GPSec	Seconds from the beginning of the GPS reference week; accurate to the millisecond level	Y
9	Receiver Status	Ulong	An eight digit hexadecimal number representing the status of various hardware and software components of the receiver (see Table 182: Receiver Status on page 781)	Y
10	Reserved	Ulong	Reserved for internal use	Y
11	Receiver S/W Version	Ulong	A value (0 - 65535) representing the receiver software build number	Y
12	;	Char	The character indicates the end of the header	N


The ASCII message data structure, of which an example is displayed in Figure 38, is described in Table 2. The first field displayed in Table 2 represents the entire header. The data structure starts from the second field. Therefore, the position of the antenna acquired as geodetic coordinates is reported respectively in field 3, 4 and 5, considering the data string displayed in Figure 38. For any further information about the data acquired from the NovAtel receivers please refer to the Commands and Logs Reference Manual (7) by NovAtel.

```
... ;SOL_COMPUTED,NARROW_INT,42.45157584163,12.39625916110,64.1749,49.1000,WGS84,0.0072,0.0065,0.0168,"0",1.100,0.000,41,37,37,36,00,21,ff,37* ...
```

Figure 38. Example of ASCII message data structure taken from Figure 36.

## Report on the activities of the European project GISCAD-OV

Table 2. ASCII message data structure (7).

Field	Field type	Description	Format	Binary Bytes	Binary Offset
1	BESTPOS header	Log header. See <i>Messages</i> on page 30 for more information.		H	0
2	sol stat	Solution status, see <i>Table 80: Solution Status</i> on the next page	Enum	4	H
3	pos type	Position type, see <i>Table 81: Position or Velocity Type</i> on page 433	Enum	4	H+4
4	lat	Latitude (degrees)	Double	8	H+8
5	lon	Longitude (degrees)	Double	8	H+16
6	hgt	Height above mean sea level (meters)	Double	8	H+24
7	undulation	Undulation - the relationship between the geoid and the ellipsoid (m) of the chosen datum  <div style="border: 1px solid black; padding: 5px; width: fit-content;">  When using a datum other than WGS84, the undulation value also includes the vertical shift due to differences between the datum in use and WGS84.         </div>	Float	4	H+32
8	datum id#	Datum ID number 61 = WGS84 63 = USER	Enum	4	H+36
9	lat $\sigma$	Latitude standard deviation (m)	Float	4	H+40
10	lon $\sigma$	Longitude standard deviation (m)	Float	4	H+44
11	hgt $\sigma$	Height standard deviation (m)	Float	4	H+48
12	stn id	Base station ID	Char[4]	4	H+52
13	diff_age	Differential age in seconds	Float	4	H+56
14	sol_age	Solution age in seconds	Float	4	H+60
15	#SVs	Number of satellites tracked	Uchar	1	H+64
16	#solnSVs	Number of satellites used in solution	Uchar	1	H+65
17	#solnL1SVs	Number of satellites with L1/E1/B1 signals used in solution	Uchar	1	H+66
18	#solnMultiSVs	Number of satellites with multi-frequency signals used in solution	Uchar	1	H+67
19	Reserved		Hex	1	H+68
20	ext sol stat	Extended solution status (see <i>Table 84: Extended Solution Status</i> on page 436)	Hex	1	H+69
21	Galileo and BeiDou sig mask	Galileo and BeiDou signals used mask (see <i>Table 83: Galileo and BeiDou Signal-Used Mask</i> on page 435)	Hex	1	H+70
22	GPS and GLONASS sig mask	GPS and GLONASS signals used mask (see <i>Table 82: GPS and GLONASS Signal-Used Mask</i> on page 435)	Hex	1	H+71
23	xxxx	32-bit CRC (ASCII and Binary only)	Hex	4	H+72
24	[CR][LF]	Sentence terminator (ASCII only)	-	-	-

The coordinates extrapolated from a single data string indicate the position of the antenna at time specified in the header message. The displacements of the antenna in time domain are obtained by extrapolating the information about position and time from every single BESTPOS string in the file. This procedure has been implemented in the MATLAB script displayed in the appendix.

### 3.5 Data transformation

Once the geodetic coordinates have been extrapolated from the log files, in order to compare the accelerometer signals (that are implicitly in a local coordinate system, where local is referred to the tested structure) with the Novatel Receiver signals, one has to convert the geodetic coordinates as explained previously. Therefore, a MATLAB script was written to implement the conversion procedure. The script is displayed in the appendix and it uses the Mapping Toolbox to convert the geodetic coordinate to local coordinates. The result consist of a matrix for each antenna. The generic column contains the coordinate of the position of the antenna in the local reference system acquired at each step. The generic row represents the position of the antenna at a precise step. Since the local reference system considers three axes, the columns that make up the matrix are three, respectively x, y and z. On the other hand, the rows are as many as the step considered in the acquisition process. The matrix displayed below (6) represent a generic output of the conversion process in which the coordinates of the position of the antenna for each step are reported.

$$\begin{bmatrix} x_1 & y_1 & z_1 \\ x_2 & y_2 & z_2 \\ x_3 & y_3 & z_3 \\ \vdots & \vdots & \vdots \\ x_i & y_i & z_i \\ \vdots & \vdots & \vdots \\ x_{n-1} & y_{n-1} & z_{n-1} \\ x_n & y_n & z_n \end{bmatrix} \quad (6)$$

In the matrix above n is the number of steps in the acquisition process. Hence, the matrix has dimensions 3xn. The resting position of each antenna can be calculated as the mean of the positions acquired at each step. In Figures [39, 42], the position of the antennas acquired by the NovAtel receivers are displayed in the ECEF-r, ENU and local reference system.

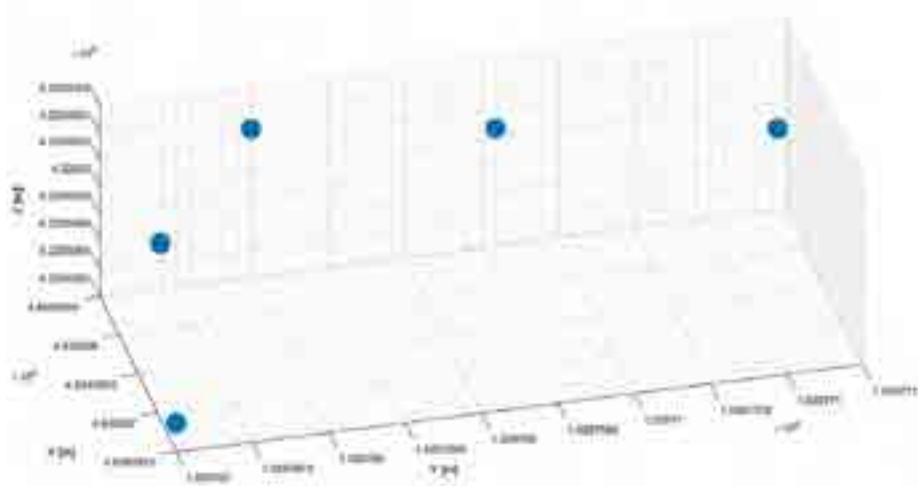


Figure 39. Position of the NovAtel antennas in ECEF-r reference system.

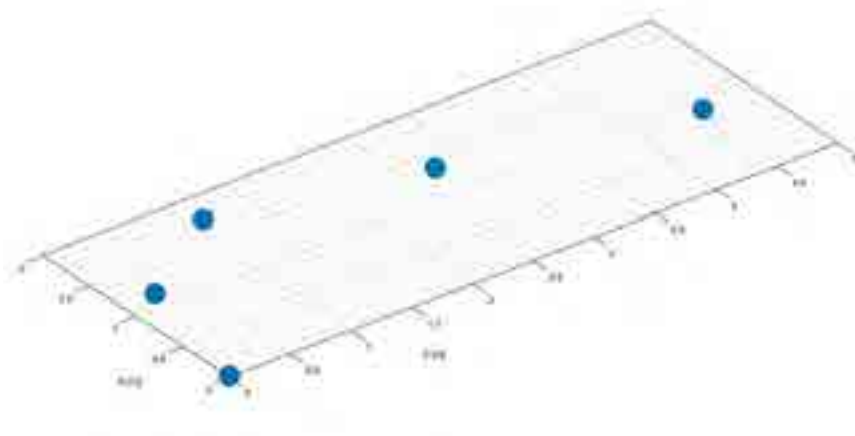


Figure 40. Position of the NovAtel antennas in ENU reference system.

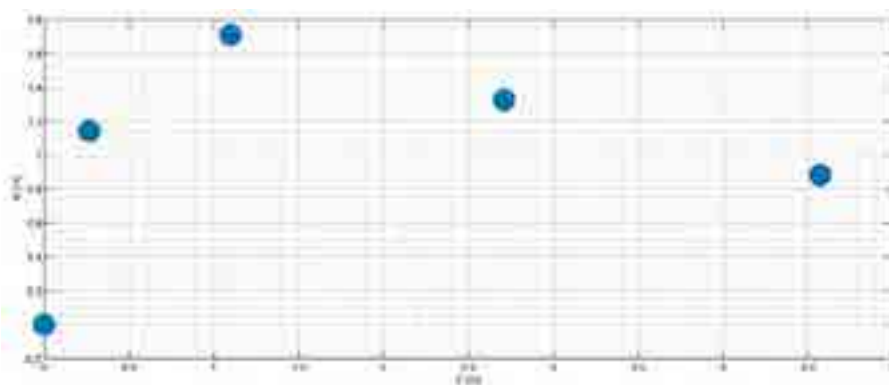


Figure 41. Position of the NovAtel antennas in EN reference system.

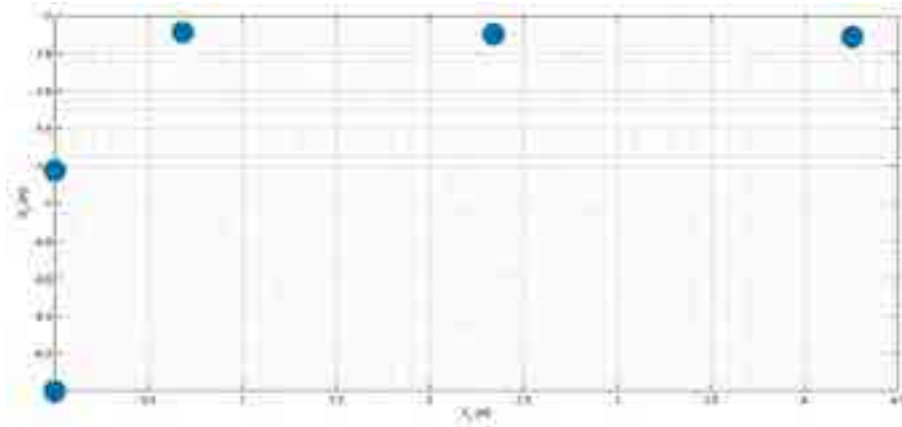


Figure 42. Position of NovAtel antennas in local reference system.

As it can be noticed, the conversion from the ECEF-r to the ENU reference system makes the plot two dimensional as it should be since the antennas were installed at the same height (Figure 40 and Figure 41). The further transformation from ENU to local coordinates aligns the position of the antennas with the local coordinate reference system of the structure (Figure 42).

As an example, Figure 43 shows the position of the first antenna during the first test. The position here shown is in geodetic coordinates. From this set of data, it was possible to calculate the position of the antenna in local coordinates by means of the equations previously shown and to calculate its displacements relatively to the resting position of the antenna, which was calculated as the mean position. The displacements of the first antenna during the first test are shown in Figure 44. As it can be noticed, the major displacements are along the y-axis, as it should be since the structure is being excited in this same direction very closely to the first monitored point.

Since the GPS signal is affected by noise, the acquired signal was furthermore transformed in order to reduce the noise. Therefore, a passband filter was implemented in a MATLAB script, which is displayed in the appendix. The result of the filtering process is shown in Figure 45. The plot depicts the final result of the GPS signal post processing, which was then used for the comparative analysis with the accelerometer results. The post processed signal clearly shows the two time gaps in which the excitement was performed.

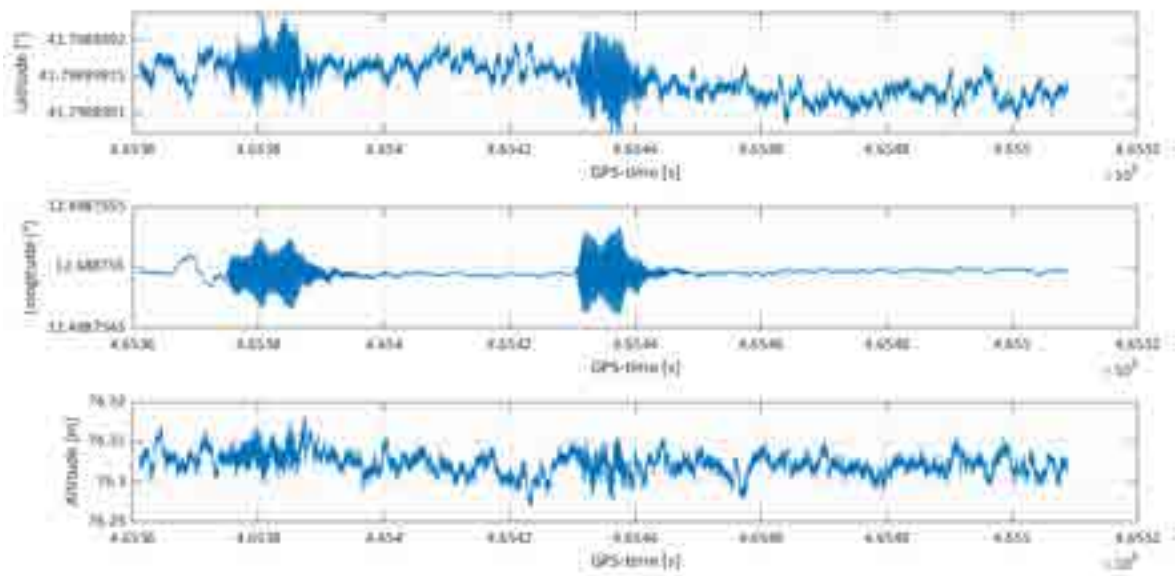


Figure 43. Position of the first antenna during the first test in geodetic coordinates.

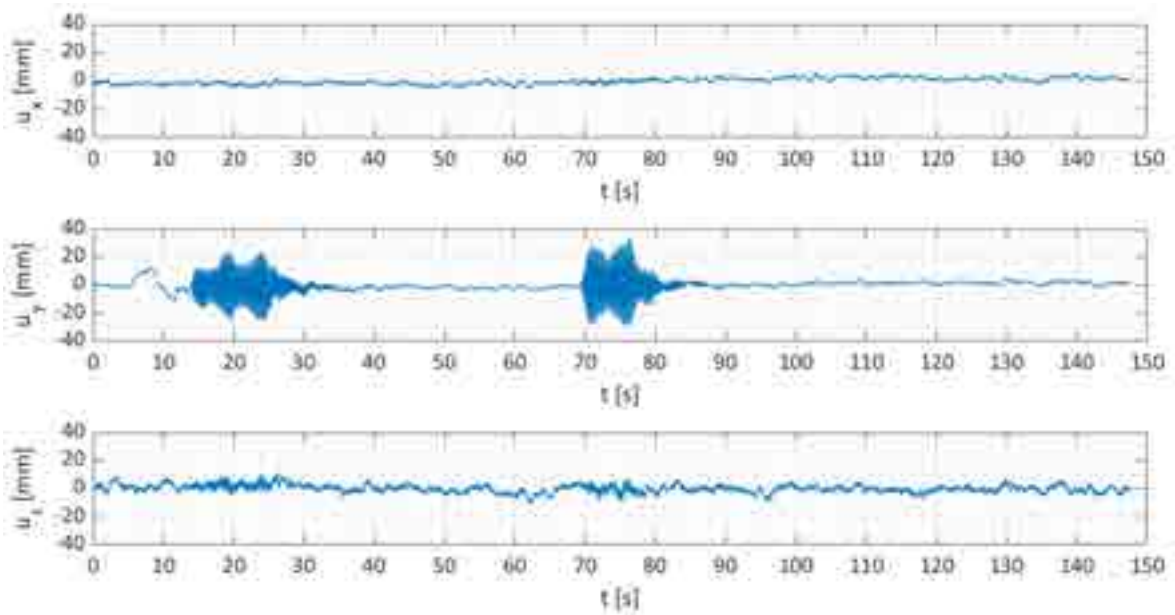


Figure 44. Displacements of the first antenna during the first test in local coordinates.



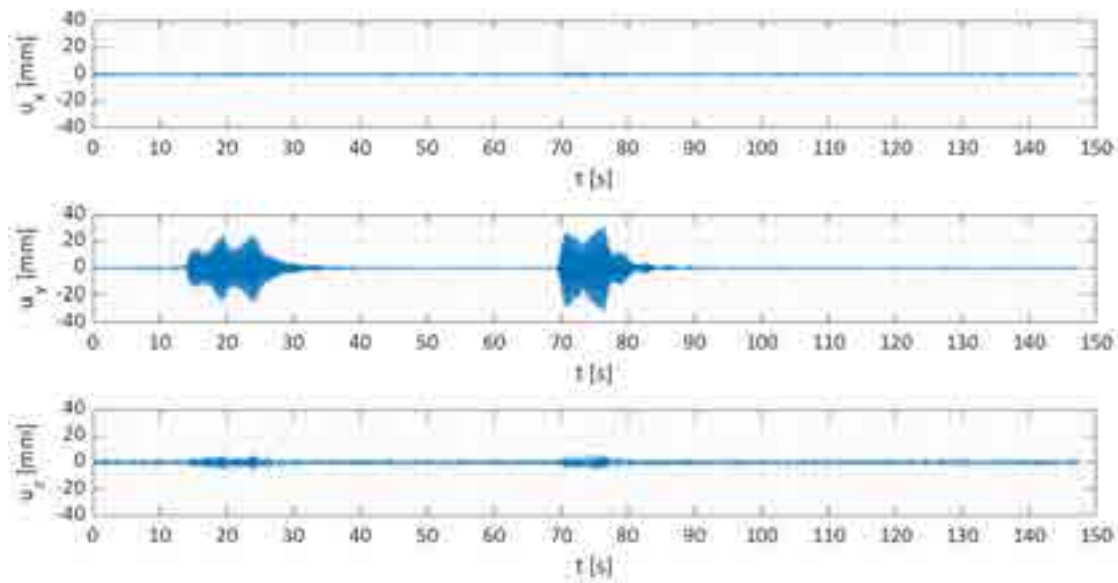


Figure 45. Filtered displacements of the first antenna during the first test in local coordinates.

### 3.6 Results

In the present paragraph, the results of the first test conducted on the small-scale benchmark structure are shown. The test consisted in acquiring the displacements of the five antennas during a dynamic excitation in the direction of the y-axis. The acquisition time was about 150 seconds. The different lengths of the acquisition time from one antenna to the other is due to the fact that the five antennas must necessarily be started and ended in series. During the whole acquisition session, the excitation was manually performed twice, close to the installation point of the first antenna and had a duration of about 10 seconds. The results are in the time and frequency domain. Indeed, the time domain results show the displacements of the antennas acquired during the test by the receivers. On the other hand, the frequency domain results were obtained from the time domain results by analysing the acquired displacements that describe the free oscillations of the structure and then calculating the structure natural frequency.

#### 3.6.1 Time domain

The time domain results are obtained by applying the method described in the previews paragraphs. Hence, the displacements of the antennas during the test are in the local reference system shown in Figure 27. According to the mode shapes of the structure, the

main displacements of the monitored points are along the out-of-plane direction, which means along the normal through the plane that contains the structure. As it can be seen from the sketch depicted in Figure 27, the first two antennas are contained in a plane with normal parallel to the y-axis while the other three antennas are contained in a plane with normal parallel to the x-axis. Therefore, the main displacements of the first two antennas are along the y-axis while the main displacements of the other three antennas are along the x-axis. This observation was used as a validation of the coordinate transformation method applied to the data.

In Figures [46, 50] the displacements of each antenna during the test are shown. The acquired displacements of the single antenna are depicted in three subplots, each representing the displacements along one of the coordinate axes of the local reference system. From the top to the bottom subplot, the displacements along the x, y and z-axis are shown respectively.

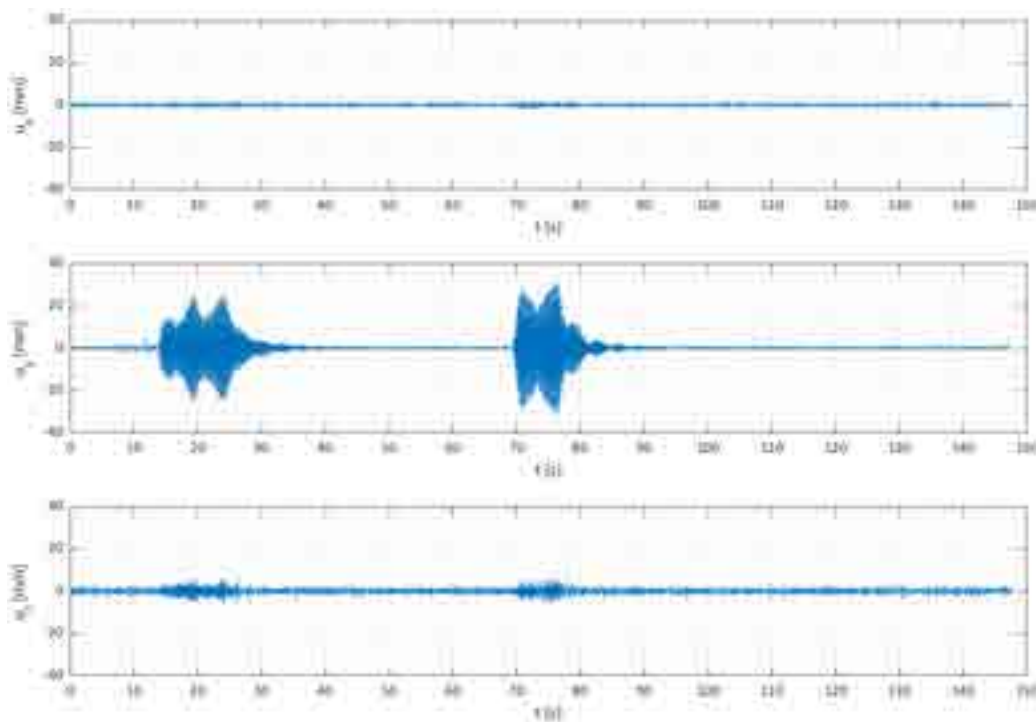


Figure 46. Displacements along the three local axes of the antenna 1.

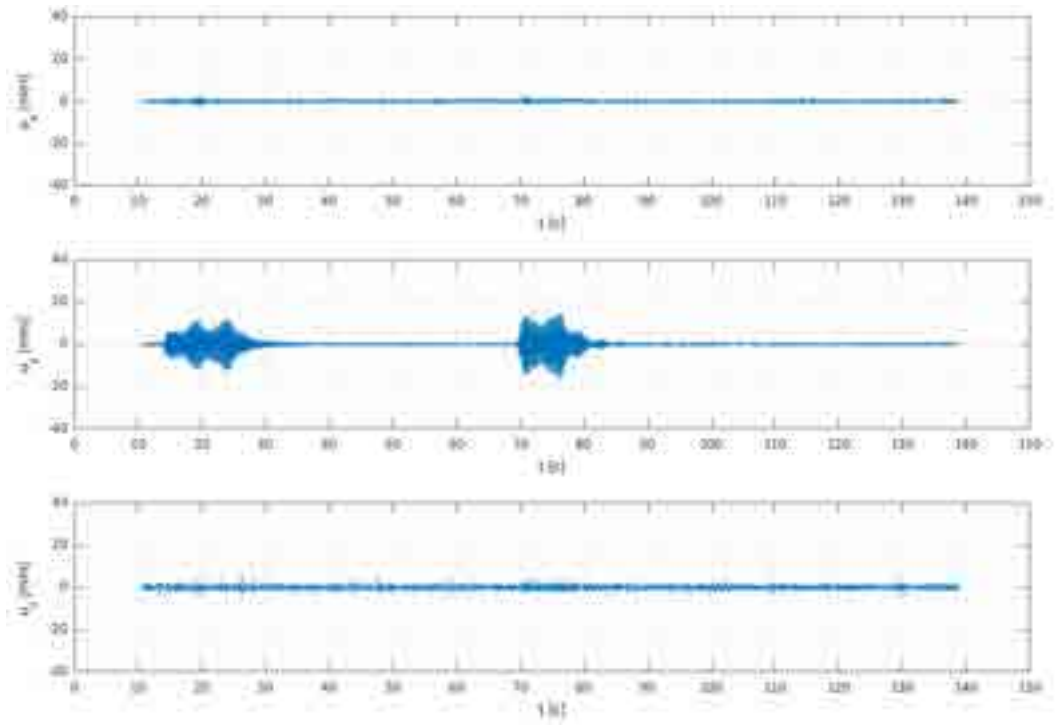


Figure 47. Displacements along the three local axes of the antenna 2.

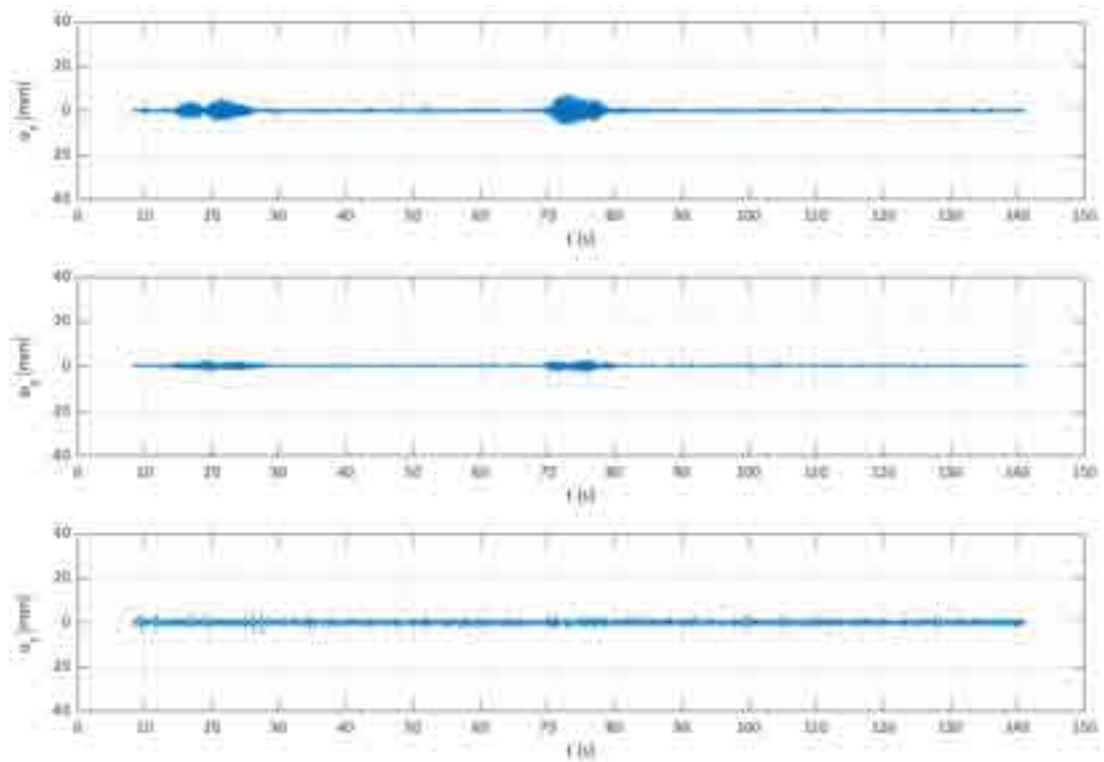


Figure 48. Displacements along the three local axes of the antenna 3.

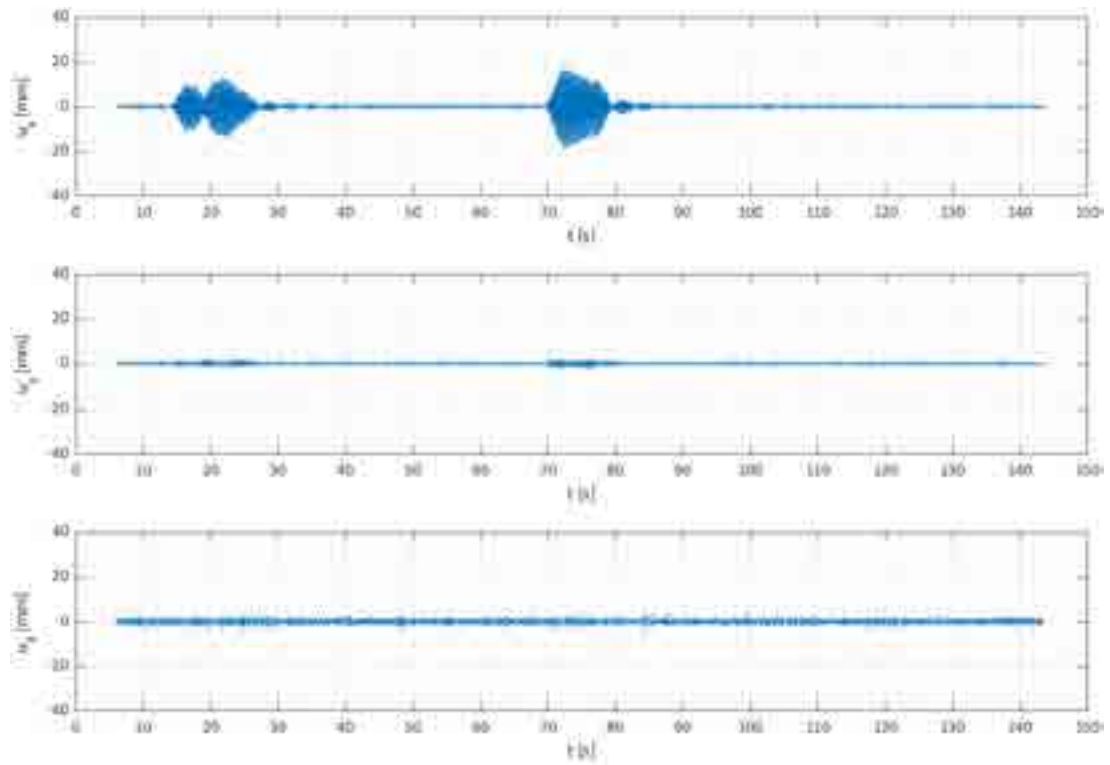


Figure 49. Displacements along the three local axes of the antenna 4.

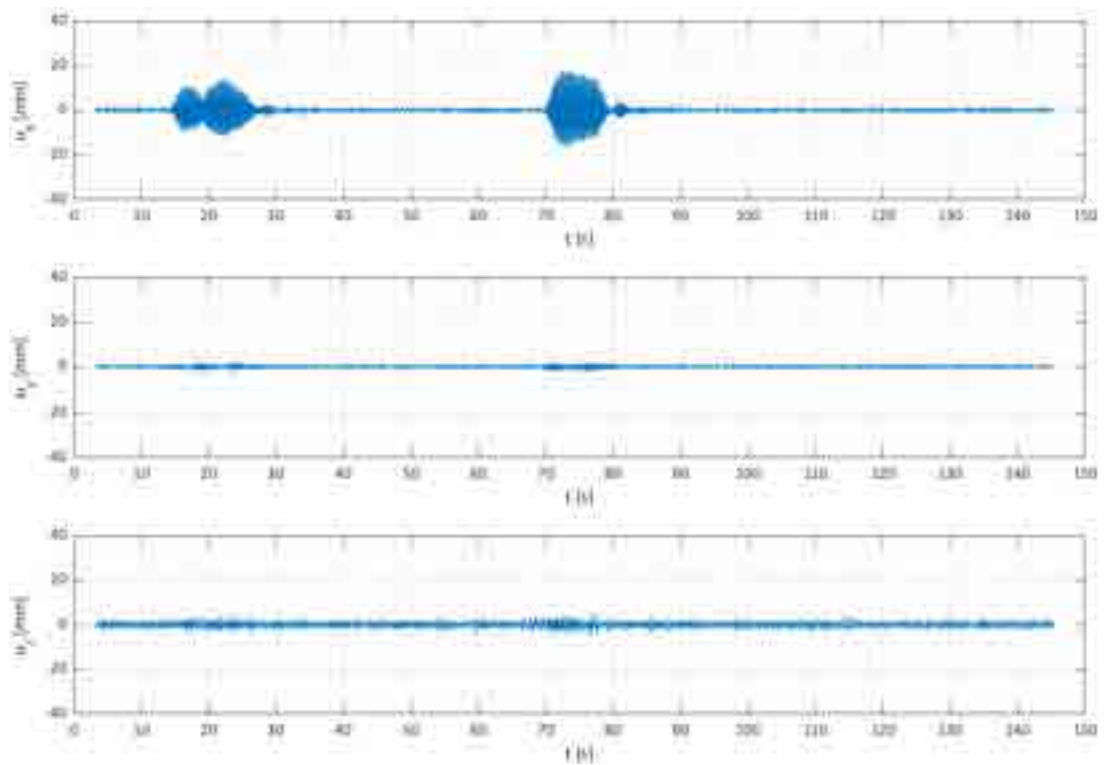


Figure 50. Displacements along the three local axes of the antenna 5.

As it can be noticed, the displacements clearly show the two excitations that were performed on the structure during the acquisition. Since the two excitations were manually performed, they slightly differ in duration and intensity. Moreover, since the excitation was performed close to the installation point of the first antenna, this was affected by the biggest displacement. On the other hand, the antennas installed near the corner of the structure (the second and the third) show very low displacements. This is because the zone in which those antennas were installed is far more rigid than the other zones, therefore preventing the antennas from big oscillations. In Table 3, the peaks of displacements for each antenna are shown, taking into consideration the two excitations.

*Table 3. Peaks of displacements.*

Antenna	Peak of displacements [mm]		Direction
	<i>Excitation 1</i>	<i>Excitation 2</i>	
1	25.4	31.6	Y
2	13.2	15.4	Y
3	5.8	7.3	X
4	12.8	17.6	X
5	14.6	18.0	X

### 3.6.2 Frequency domain

The frequency domain results were obtained directly from the analysis of the time domain results. In particular, the free oscillations of the structure were considered in order to evaluate the structure natural frequency. As shown in Figure 51, the acquired signal can be roughly divided in three main parts, being the first one the range of signal affected by noise, the second one the range of signal affected by the excitation and the third one the range of signal containing information about the free oscillations. While the first two parts can be easily identified with naked eye, the third part cannot. Therefore, this part of signal has been highlighted in green in the figure below. The free oscillations start when the forced oscillations stop and the system begins oscillating with its natural frequency. Hence, the range of signal of interest approximately starts when the excitation stops and ends when the free oscillations are completely damped. The two highlighted zones have been given the name of range 1 and range 2 respectively.

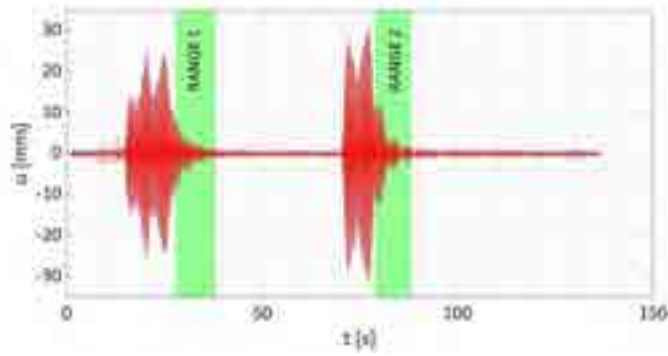


Figure 51. Signal range (highlighted in green) of the NovAtel signal containing information about the free oscillations of the system.

This range of signal was analysed with MATLAB by using the CPSD function which estimates the cross power spectral density of two discrete-time signals,  $x$  and  $y$ , using Welch's averaged, modified periodogram method of spectral estimation (9). By applying the function on the same signal, the power spectral density is obtained (PSD). This gives us information about the natural frequency of the oscillator system being studied, which in this case is the structure. In Figure 52 and Figure 53 the PSD of each antenna is shown, calculated for both the signal ranges respectively. As it can be noticed, the highest peak was shown by the first antenna while the lowest by the third antenna. This observation is reasonable since the first antenna is the closest to the excitation point, while the third antenna is the closest to the corner of the structure, which, as already underlined, is the stiffer part of the structure. The results are grouped in Table 4 and Table 5, in which the frequency peaks and the mean frequency peaks are shown.

Table 4. Peak frequencies.

Antenna	Peak frequency [Hz]	
	Excitation 1	Excitation 2
1	4.6	4.56
2	4.6	4.56
3	3.3	4.22
4	4.3	4.22
5	4.6	4.22

Table 5. Mean peak frequencies.

Mean peak frequency [Hz]	
Excitation 1	Excitation 2
4.53	4.36

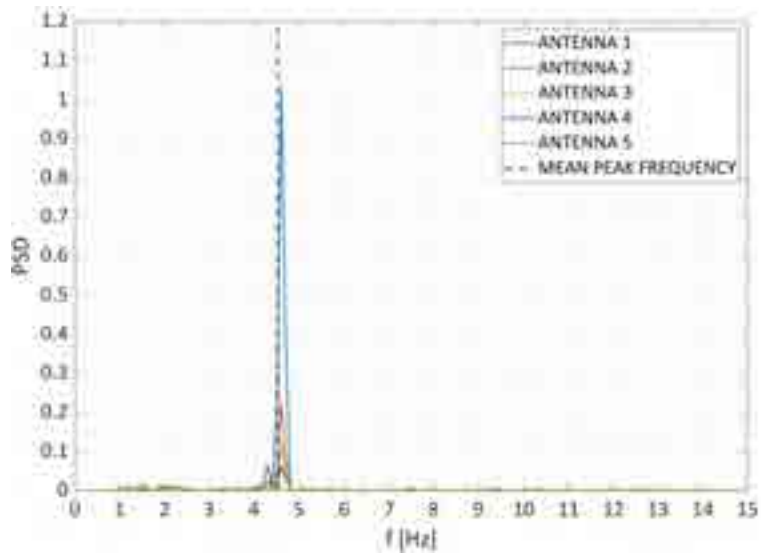


Figure 52. PSD of range 1.

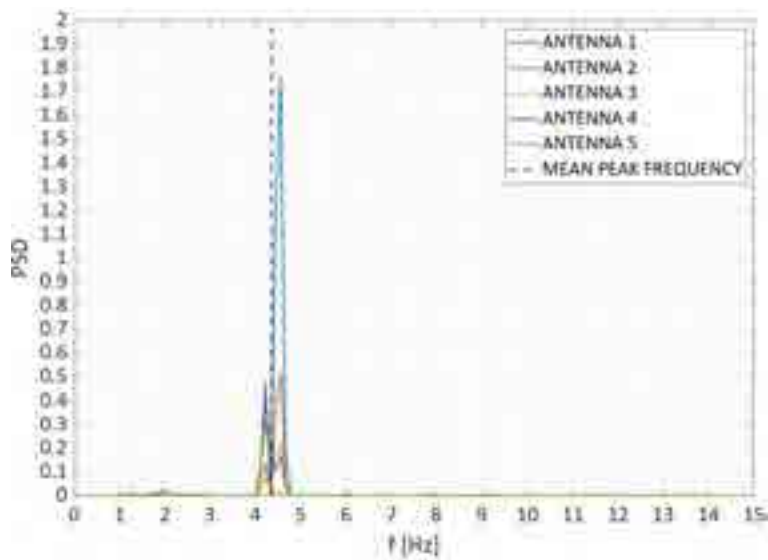


Figure 53. PSD of range 2.

With the goal of testing the precision of the NovAtel system, the so calculated natural frequency was compared with the result of the modal analysis conducted on the FEM model of the structure. As shown in Table 6, the difference between the FEM model and the post-processed data in terms of natural frequency is about the 13%. Even though this difference could seem big, it must be taken into account that the FEM model has not been calibrated yet.

*Table 6. Comparison between the NovAtel signal and the FEM model in the frequency domain.*

Natural frequency calculated from NovAtel signal [Hz]	Natural frequency of the FEM model [Hz]	Percentage difference [%]
4.45	5.11	12.92

### 3.7 Comparison with accelerometric system

The acquired satellite data was then compared to the accelerometric data in order to analyse the efficiency of the NovAtel system. Time synchronization between the accelerometric and the NovAtel signals has been performed using the reference time indication in the BESTPOS strings of the Novatel Receivers logs. Moreover, GPS time is not adjusted to match the rotation of the Earth, so it does not contain leap seconds or other corrections that are periodically added to UTC. GPS time was set to match UTC in 1980, but has since diverged. As of January 2017, GPS time is 18 seconds ahead of UTC (10). Therefore, a further correction was made to the GPS time by subtracting 18 seconds from the time data acquired in order to synchronise the accelerometer and the antenna signals. Figure 54 shows the two type of signals that were acquired during the test. The NovAtel signal is depicted in red, while the accelerometric signal id depicted in blue. The main difference between the two set of data is that the NovAtel signal shows the antenna's displacement while the accelerometric signal shows the acceleration of the accelerometer. Therefore, the two set of data cannot be compared without a first post processing of one of the signals, such as a double numerical integration of the accelerations or a double numerical differentiation of the displacements. As it can be noticed from the acquired signals without post processing depicted in the figure below, both monitoring systems detect the two excitations that were manually performed on the structure. Moreover, the



two signals appear to be synchronized, which means that the starting and ending point of the excitation is the same for both signals. Hence, the NovAtel system was able to detect the excitation performed on the structure.

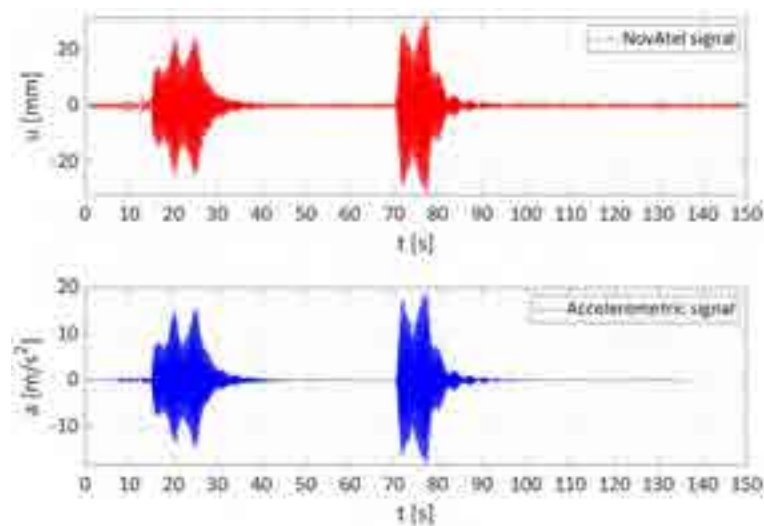


Figure 54. Comparison between the NovAtel and the accelerometric data.

In order to proceed with the comparison between the two set of data, the accelerations were integrated twice to obtain the displacements. Hence, a first comparison between the two monitoring systems was made by comparing the displacements acquired. Then, a second comparison was carried out by comparing the natural frequency of the structure calculated by the two systems. This was calculated by applying a Fast Fourier Transform based algorithm on the free oscillations of the system acquired by the two systems.

### 3.7.1 Displacements' comparison

The accelerations acquired by the accelerometric system have been integrated twice in order to evaluate the displacements. The experimental displacements are computed from the recorded acceleration via a double numerical integration, provided the velocities first and then the accelerations, according to the Simpson's rule for numerical integration and the application of a suitable fourth order band-pass filter, Butterworth type. In the integration process, a pass band filter with range 0-25 Hz was used. The higher bound was

chosen in order to set the same conditions of the satellite receivers. Indeed, these sample at a rate of 100 Hz, which means they see frequencies from 0 Hz and up to 25 Hz.

The displacements were then compared with the acquired NovAtel data. Figures [55, 59] show the comparison between the displacements acquired from the NovAtel receivers (in red) and the displacements evaluated from the accelerometric data (in blue) for each point that was monitored. As it can be noticed, there are strong similarities between the two types of signals, both highlighting displacements of the same order of magnitude.

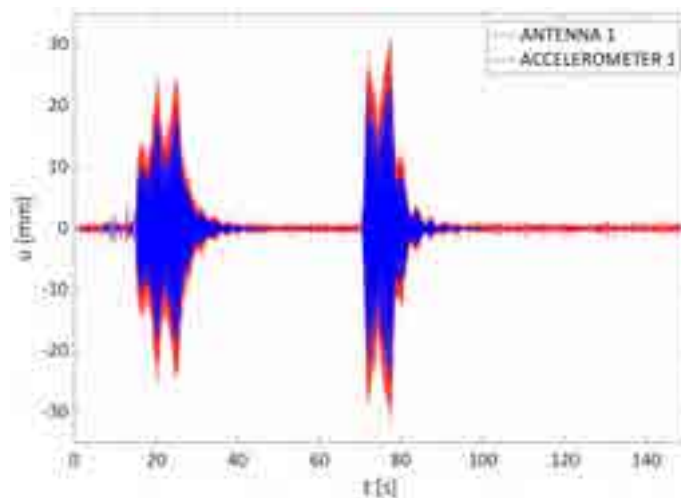


Figure 55. Comparison between the first antenna and accelerometer.

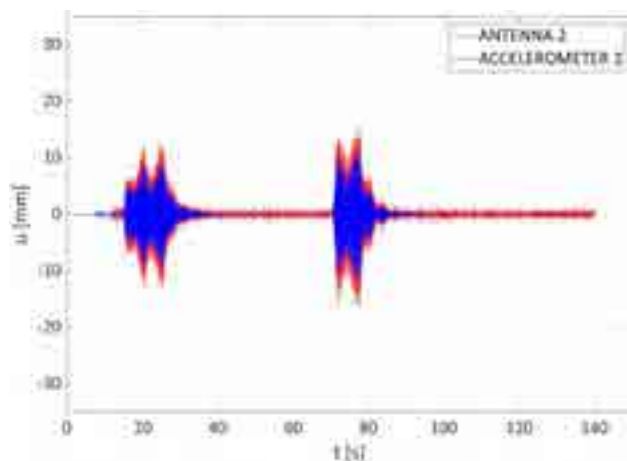


Figure 56. Comparison between the second antenna and accelerometer.

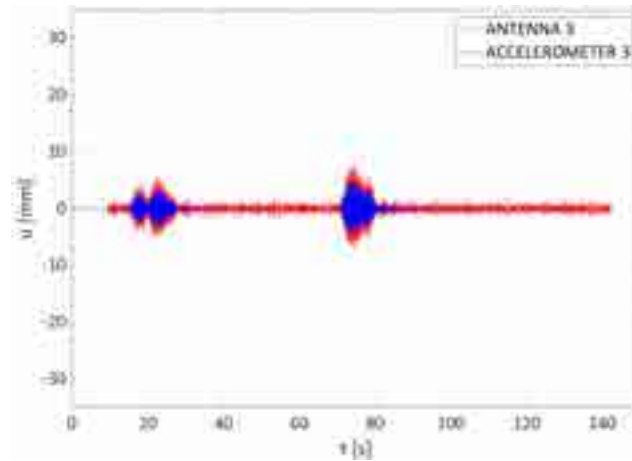


Figure 57. Comparison between the third antenna and accelerometer.

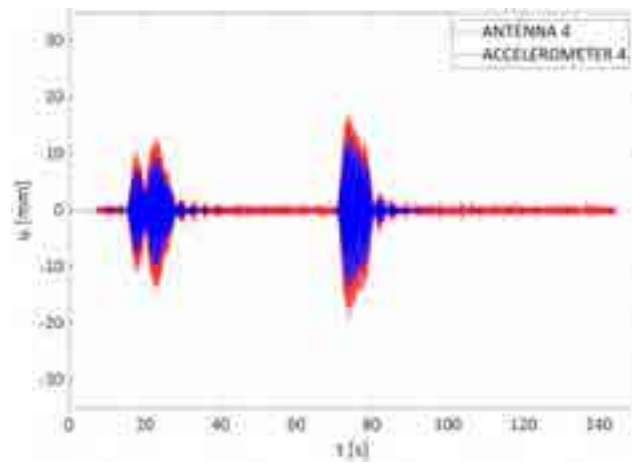


Figure 58. Comparison between the fourth antenna and accelerometer.

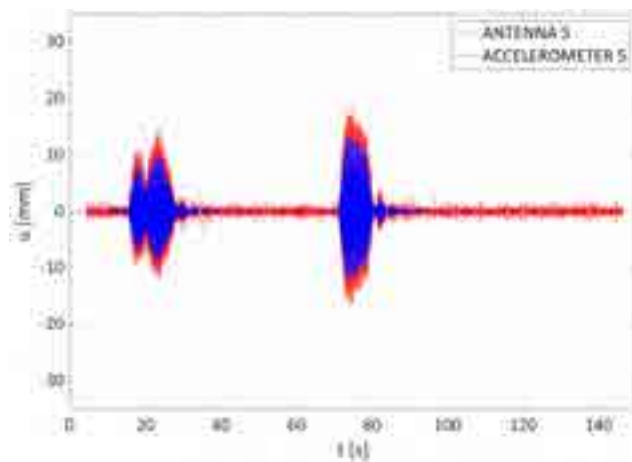


Figure 59. Comparison between the fifth antenna and accelerometer.

## Report on the activities of the European project GISCAD-OV

Table 7 shows the comparison between the peaks of displacements that were acquired by the two monitoring systems. Table 8 shows the differences between the NovAtel and accelerometric system in terms of peak of displacements. Table 9 shows the mean difference between peaks of displacements. These tables highlights a mean difference of the same order of magnitude of the noise of the satellite signal. It is reasonable to think that a denoising procedure, such as the wavelet theory, applied to the satellite signal would improve the quality and the accuracy of the NovAtel system. Tests are ongoing.

Table 7. Peaks of displacements acquired by the two monitoring systems.

Monitored point	Peak of displacements [mm]			
	Excitation 1		Excitation 2	
	Antenna	Accelerometer	Antenna	Accelerometer
1	25.4	18.7	31.6	24.9
2	13.2	8.9	15.4	11.4
3	5.8	3.4	7.3	4.7
4	12.8	9.1	17.6	12.7
5	14.6	9.9	18.0	13.2

Table 8. Differences between the two monitoring systems in terms of peaks of displacements.

Monitored point	Difference between NovAtel and accelerometric signal in terms of peaks of displacements [mm]	
	Excitation 1	Excitation 2
1	6.7	6.7
2	4.3	4
3	2.4	2.6
4	3.7	4.9
5	4.7	4.8

Table 9. Mean difference of peaks of displacements between the two monitoring systems.

Mean difference between peaks of displacements [mm]	
Excitation 1	Excitation 2
4.36	4.6

### 3.7.2 Frequencies' comparison

In order to proceed with the comparison between the accelerometric and the NovAtel system in the frequency domain, both signal had to be post processed to obtain the natural frequency. The method used in the previous paragraphs to obtain the natural frequency of the structure was applied on both set of data. Figure 60 shows the range of signal (highlighted in green) that was taken into account to evaluate the PSD. The first range contains the free oscillations due to the first excitation, while the second range contains the free oscillations due to the second excitation. Figure 61 and Figure 62 show the peak frequencies evaluated from the NovAtel and accelerometric signal for both manual excitations respectively.

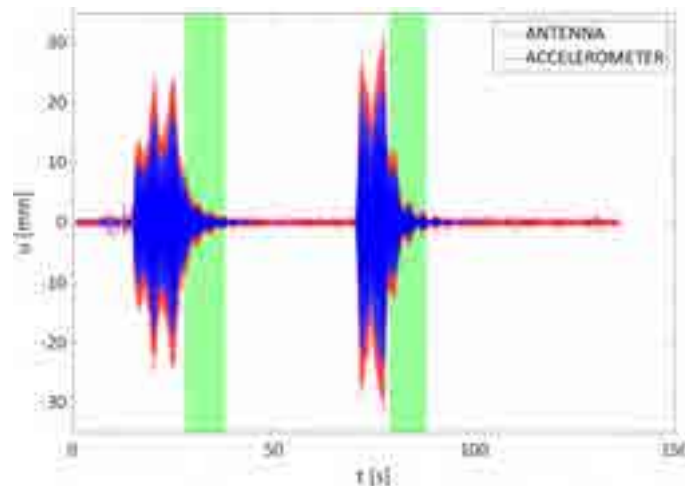


Figure 60. Signal range (highlighted in green) of the NovAtel and the accelerometric system containing information about the free oscillations of the system.

The results about the peak frequency for each monitoring system are shown in Table 10. Table 11 shows the differences between the peak frequencies evaluated by the NovAtel and the accelerometric system respectively. Table 12 shows the mean difference between the two monitoring systems in terms of peak frequencies. As it can be noticed from the tables, the same peak frequencies were evaluated from the signals acquired by the two monitoring systems. The only exception is the peak frequency evaluated from the free oscillations of the third monitored point caused by the first excitation. Indeed, since the point being monitored was very close to the corner of the structure, which can be

reasonably considered as a very rigid zone of the structure, the displacements acquired were very low. This had the consequence that the free oscillations of the point and the signal noise showed almost the same order of magnitude. Hence, the NovAtel system failed in the acquisition of the free oscillations, leading to a wrong evaluation of the peak frequency. This did not happen when the same point was tested with the second manual excitation because this was slightly stronger, causing bigger displacements of the monitored point.

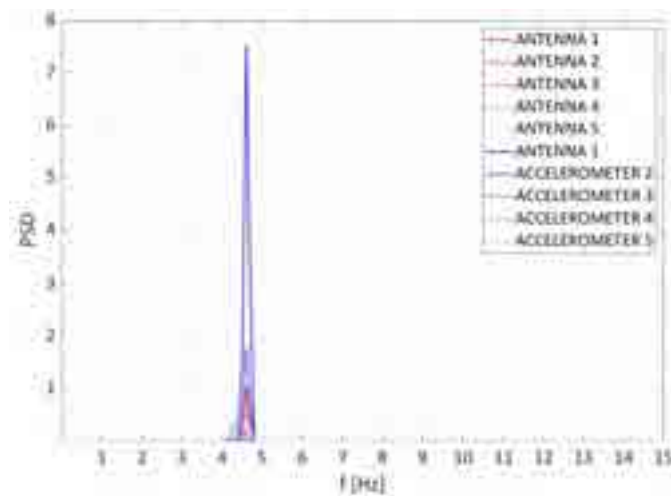


Figure 61. Comparison between the PSD of the NovAtel and accelerometric signals, considering the free oscillations due to the first excitation.

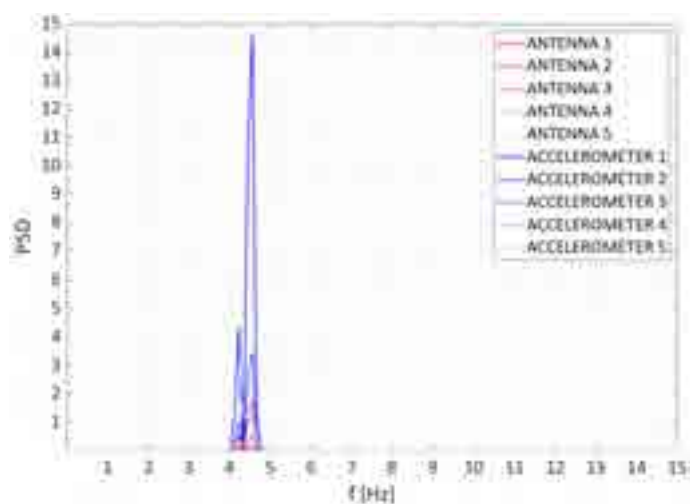


Figure 62. Comparison between the PSD of the NovAtel and accelerometric signal, considering the free oscillations due to the second excitation.

## Report on the activities of the European project GISCAD-OV

Table 10. Peak frequencies of the NovAtel and accelerometric system.

Monitored point	Peak frequency [Hz]			
	Excitation 1		Excitation 2	
	Antenna	Accelerometer	Antenna	Accelerometer
1	4.6	4.6	4.56	4.56
2	4.6	4.6	4.56	4.56
3	3.3	4.3	4.22	4.22
4	4.3	4.6	4.22	4.22
5	4.6	4.6	4.22	4.22

Table 11. Differences of the peak frequencies between the NovAtel and the accelerometric system.

Monitored point	Difference between NovAtel and accelerometric signal in terms of peak frequency [Hz]	
	Excitation 1	Excitation 2
1	0	0
2	0	0
3	1	0
4	0.3	0
5	0	0

Table 12. Mean difference of the peak frequencies.

Mean difference between Peak frequencies [Hz]	
Excitation 1	Excitation 2
0.26	0

## 4 Monitoring of a full-scale benchmark structure

T5.6 consisted of the monitoring of a new benchmark structure in order to validate the results of the Pilot Project. For this purpose, the GPS+Galileo HAS system was mounted on a full-scale benchmark structure. The task aims to investigate the efficiency of the monitoring system when a real case application is considered such as a road bridge. The methodology already tested in T4.3 was applied again to the present task. The main difference between the two tasks is that in this case the vertical displacements, instead of the horizontal ones, are being acquired.

### 4.1 Structure description

In order to proceed with the validation process a road bridge was chosen as a full-scale benchmark structure. The bridge is located near the city of Orte (VT) and links the two-lane national road SS675 over the river Tiber. The structure consists of a multi span bridge made of prestressed concrete. The static system that describes the behavior of the single span of the road bridge is that of a simply supported beam, 40m long, with a distributed load representing its weight. Figure 63 illustrates the static system of the road bridge, being  $L$  the length of the span,  $w$  the linear distributed load,  $T$  the shear force and lastly  $M$  the bending moment.

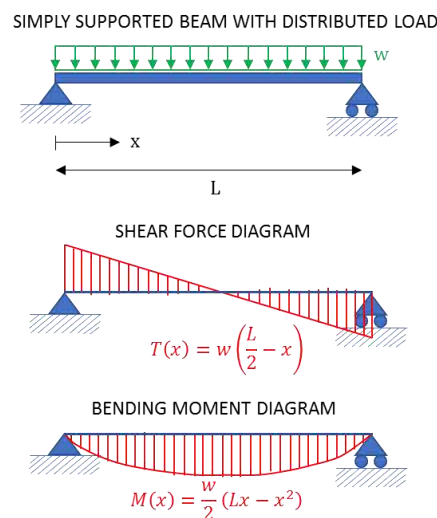


Figure 63. Static system of the bridge road.



The reinforced concrete deck is composed of four box girders. The monitoring system was tested with the normal traffic conditions and was installed on the second span of the bridge since the national company ANAS that has in charge the management of the road bridge is already monitoring it. Hence, the model and the results refer only to the second span. Figures [64, 69] illustrate the benchmark structure considered for T5.6.



*Figure 64. Drone view of the road bridge.*



*Figure 65. Drone view of the second span of the bridge.*



*Figure 66. View of the road from on top of the deck.*



*Figure 67. View from below the deck of the four box girders and the two piers that supports the second span.*



*Figure 68. Details of the four box girders.*



*Figure 69. Details of the pier.*

## 4.2 Structure modelling

As we did for the first benchmark structure, the bridge was surveyed with laser scanner technique producing several point clouds. Differently from what was done for the first benchmark structure, the 3D FEM model of the road bridge already exists. Indeed, ANAS, the national company that has in charge the management of the road bridge, already implemented a numerical model that can be used for our purpose. Therefore, the point cloud obtained by the 3D survey is useful to refine the FEM model that already exists. The modelling process is still ongoing and so far, only the 3D survey has been carried out. Figures [70, 73] show different views of the cloud point that resulted from the 3D survey.



*Figure 70. Cloud point, shade of grey view of the second span.*



*Figure 71. Cloud point, reflected light intensity view of the second span.*

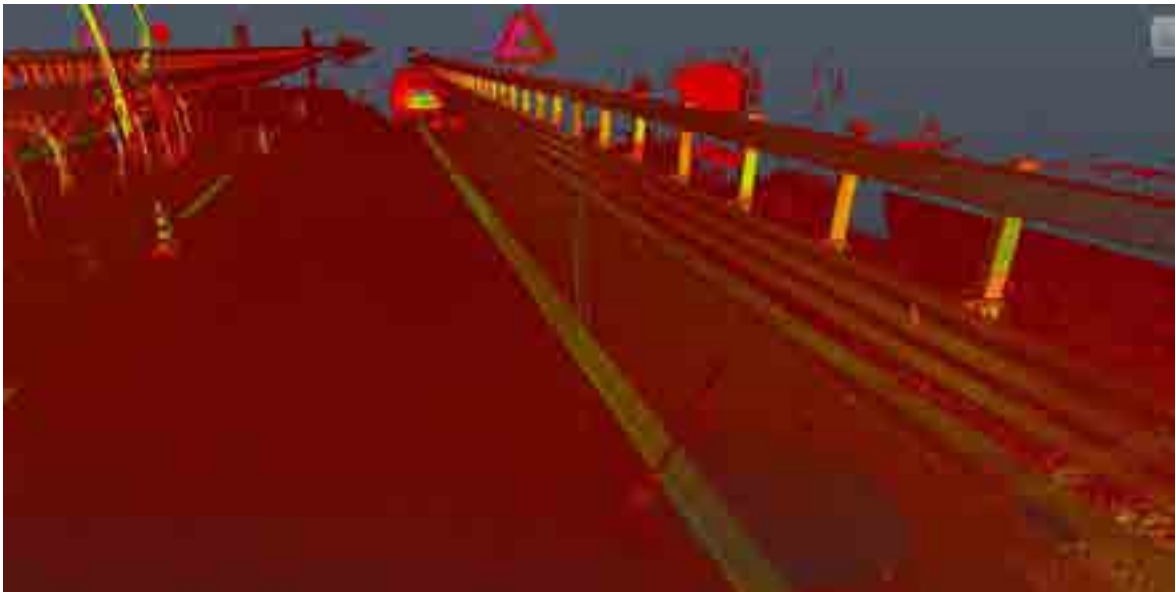


*Figure 72. Cloud point, reflected light intensity view of the road.*



*Figure 73. Cloud point, reflected light intensity view of the monitored point.*

### 4.3 Monitoring system installation

The full-scale benchmark structure was monitored with both the accelerometers and the GPS+Galileo HAS system, as already did for the small-scale benchmark structure. Thanks to ANAS, the road was partially closed to traffic in order to secure the installation process of the monitoring system. Figure 74, Figure 75 and Figure 76 show the worksite that was organized by ANAS. After the zone was secured, the installation of the monitoring systems followed. The installation of the accelerometers was carried out by the DPC. The installation of the GPS+Galileo HAS system was carried out thanks to Sogei and UNIROMA3. Both systems were employed to monitor the same points of the structure, in order to assess the efficiency of the satellite system by comparison. Figure 77 and Figure 78 show the two different monitor systems installed on the guardrail that borders the road lane. Since the antennas need open space in order to capture the radio signal from the satellites without disturbances, those were necessarily fixed on top of the guardrails as shown in the figures below. To make sure that the displacements of the top part of the guardrail would not be affected by the deformation of the guardrail itself, the DPC conducted a campaign of data acquisition in order to compare the displacements of the top and bottom part of

the guardrail, being the latter integrated to the bridge. The campaign consisted of mounting two accelerometers on the same guardrail, one on the top part and one on the bottom part. Figure 79 and Figure 80 show the configuration chosen for the two accelerometers by the DPC. The results showed that the vertical displacements of the two monitored zones were the same, meaning that in order to acquire the vertical displacements of the bridge the antennas could be installed on the top part of the guardrail.



Figure 74. First view of the worksite.



Figure 75. Second view of the worksite.



Figure 76. Third view of the worksite.



Figure 77. Antenna installed on guardrail.





*Figure 78. Antenna and accelerometer installed on the guardrail in order to monitor the same point.*



*Figure 79. Accelerometer mount on the top part of the guardrail.*



*Figure 80. Accelerometer mount on the bottom part of the guardrail.*

Differently from T4.3, a set of three antennas were used. The number of antennas involved in the test depended firstly on the availability of the instrumentation since different Pilot Projects were carried out in Europe at the same time, secondly, on how many critical points had to be monitored in order to efficiently assess the integrity of the structure. According to the static system reported in Figure 63, it was decided to employ three antennas to monitor critical points of the bridge. Hence, two antennas were mount at the centre line of the bridge, one on the right side guardrail and one on the left side one. A third antenna was mount at a quarter of the span length on the right side guardrail. Figure 81 shows a schematic representation of the plan view of the bridge on which the monitored points are highlighted. In the picture, the shear force and the bending moment of those points are also illustrated, according to the static system of that of a simply supported beam. Figures 82, 84] show the configuration of the three antennas. Only one accelerometer was employed this time that was installed to monitor point 2.

Report on the activities of the European project GISCAD-OV

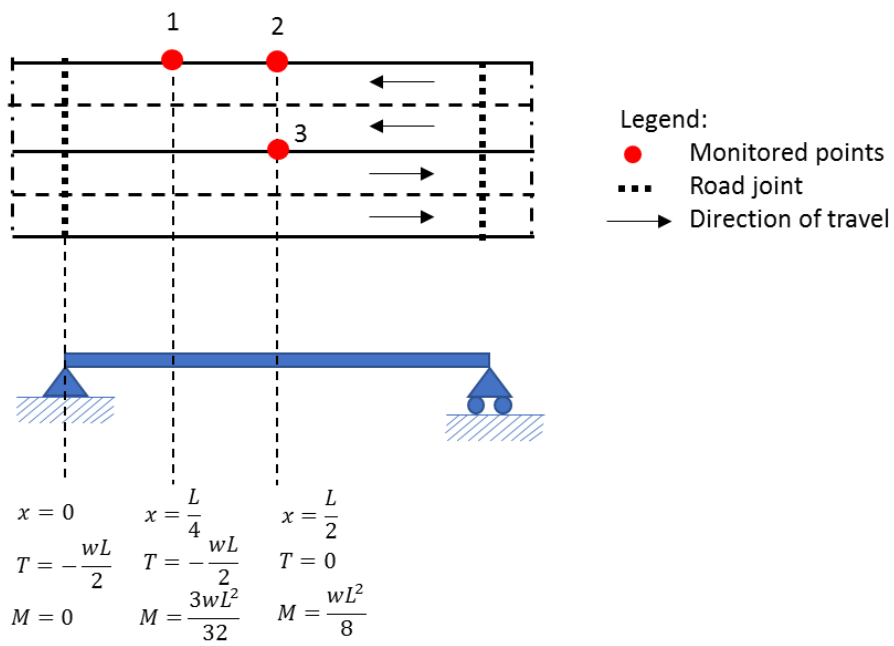


Figure 81. Schematic representation of the plan view of the bridge, being the position of the three antennas highlighted.



Figure 82. View of the antennas installed in the first (in foreground) and the second monitored point (in background).



Figure 83. View of the antennas installed in the first (in background) and the second monitored point (in foreground).



Figure 84. View of the antenna installed in the third monitored point.

#### 4.4 Results

In the present paragraph, the results obtained from the test conducted on the full-scale benchmark structure are shown. The test consisted of monitoring the road bridge with normal traffic conditions. Indeed, the monitoring systems (accelerometers and G-HAS) were mounted on the structure and left in position for about two weeks. In this period, the two monitoring systems acquired in continuous, organizing data in 1 hour interval measurements. As already did for the measurements acquired from the test conducted on the small-scale benchmark structure, the position of the antennas had to be post processed. Figure 85 shows an example of the data acquired during the test. Data here shown refers to 1 hour interval measurements that were acquired from 1:31AM to 2:31AM on September 24. The position is in geodetic coordinates, which means that before proceeding with the comparison one has to transform the coordinates.

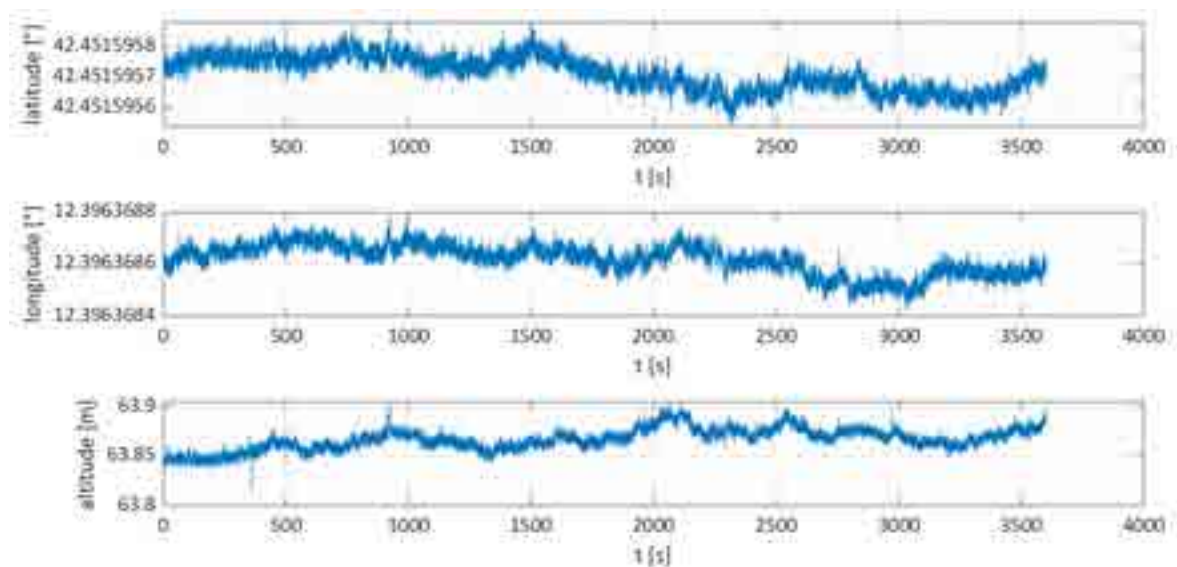


Figure 85. Position of the antenna 2 in geodetic coordinates.

Figure 86 shows the vertical displacements of the second antenna. Those were directly obtained from the acquired position in geodetic coordinates. Indeed, a coordinate transformation was applied in order to change the reference system from geodetic to local. After this, the resting position of the antenna was subtracted to the data in order to

calculate the displacements. Once more, the resting position was obtained as the mean of the positions acquired. The horizontal displacements are not shown since the test considered only the investigation of the G-HAS system efficiency in the acquisition of the vertical displacements of the road bridge. The satellite signal shows a noise of the order of magnitude of about 10 mm. It also shows some upward false peaks whose nature is being studied.

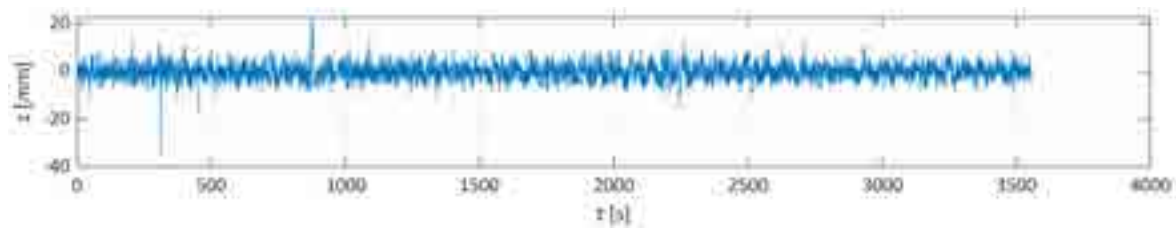


Figure 86. Vertical displacements of antenna 1 in local coordinates.

#### 4.5 Comparison with accelerometric system

In order to prove the efficiency of the system, the results were then compared to the ones obtained from the accelerometers. Before proceeding with the comparison, it was necessary to calculate the displacements from the acquired accelerations via double integration. Furthermore, data had to be synchronized since the two monitoring systems refer to UTC and GPS time. Once the necessary transformations were made to the two set of data, the comparative analysis could be made. Differently from the first test conducted on the small-scale benchmark structure, the comparison could only be made in the time domain. Indeed, the displacements that are being analyzed in the present paragraph are far lower and more impulsive than the ones analyzed in the previous chapter, make it hard to recognize the natural oscillations of the bridge. This difference is due to the type of excitation the structures were subjected to. The small-scale benchmark structure was manually excited for about 15 seconds in order to generate horizontal displacements of the order of magnitude of 5cm. The acquired signal made it possible to easily distinguish forced oscillations from natural ones. The frequency content of the natural oscillations was evaluated in order to calculate the frequency of the principal vibrational mode of the

structure. In the present case, the structure is subjected to the excitation due to the crossing of vehicles, which generates vertical displacements of the order of magnitude that varies from 10 mm to 40 mm, depending on which type of vehicle crossed the bridge. Since the order of magnitude of the noise is bigger when vertical displacements are being analyzed (about 10 mm compared to 5mm noise amplitude of horizontal displacements), the only displacements that could be measured were the ones due to the crossing of heavy vehicles such as fully load trucks. Besides the difficulty in acquiring the displacements, the type of excitation that the structure is subjected to is very impulsive, resulting in a very short structural response. Moreover, the structure being analyzed dissipates almost instantaneously the oscillations. In conclusion, even when we manage to acquire the vertical displacements, those appear as a very short gap signal making it impossible for us to distinguish forced oscillations from natural ones. Hence, the only comparison that could be made from this test was in the time domain, meaning that the displacements acquired by the two monitoring systems were compared. Figure 87 shows the superimposition of the displacements acquired by the accelerometric system and the second G-HAS receiver. Both systems monitored the same point, which is the point located at the center line of the bridge on its right side, indicated with number 2 in Figure 81. It can be noticed the higher noise that the satellite signal suffers from, resulting in the impossibility of capturing small displacements that instead, the accelerometric system manage to acquire. Indeed the displacements acquired by the accelerometric system (in blue) show peaks of displacements of the order of magnitude even lower than 5 mm. The information about those displacements is completely lost in the satellite signal (in red) due to the noise. The only displacements that can be compared are those of the order of magnitude higher than 10 mm.

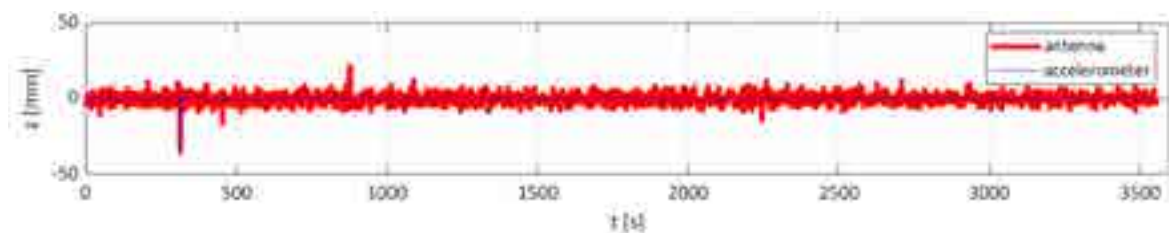


Figure 87. Comparison of the displacements acquired by the accelerometric and the G-HAS system.

Figure 88 shows the same signal previously analyzed, focusing on the first 500 second of acquisition in which a peak displacement of order of magnitude of about 40 mm was captured. The satellite signal was able to perfectly capture the instant when the peak displacement appeared and its amplitude. Even with vertical displacements the satellite signal seems to behave efficiently, as long as the displacements are higher than the noise order of magnitude.

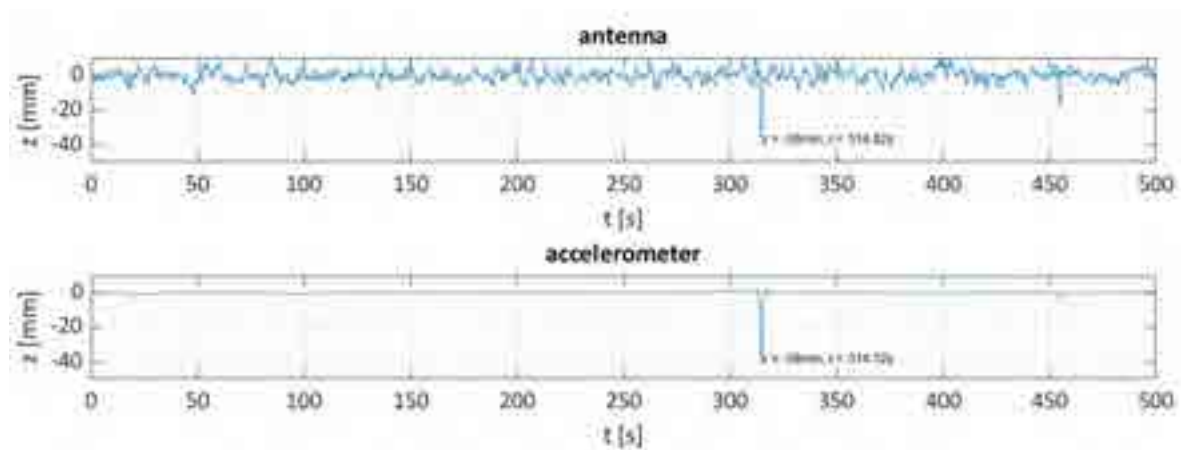


Figure 88. Comparison of the peak displacement.

Figure 89 illustrates the displacements of the three antennas and the accelerometer used to monitor the bridge. Since the antennas were mounted in different spots of the bridge, it was reasonable to expect different amplitudes of the peak displacements. On the other hand, due to the impulsive nature of the excitation, we expected from all three antennas to show the peak displacement at almost the same time. Our expectations were right as it can be seen from the figure below.



# Report on the activities of the European project GISCAD-OV

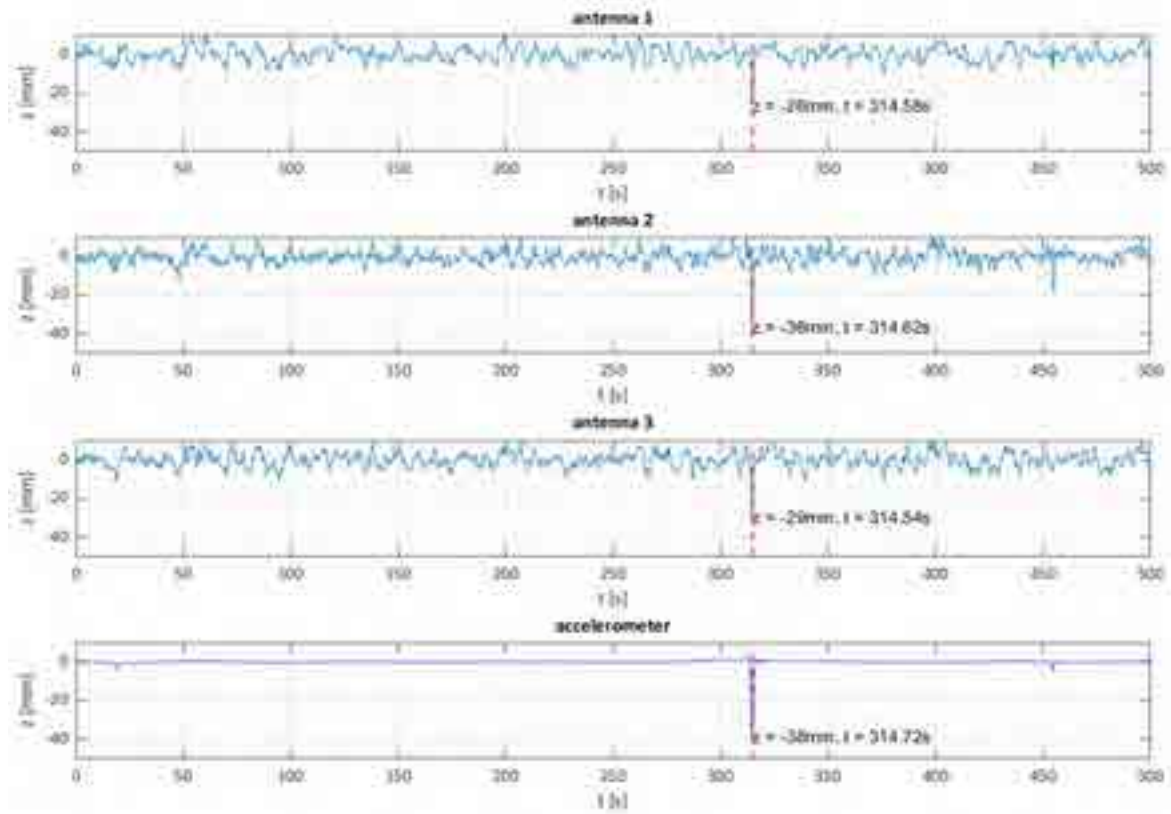


Figure 89. Comparison of the peak displacements of all the sensors mounted on the bridge.

## 5 Appendix

### 5.1 Script for log files reading

```

clear
close all
clc

di rn = 'test160421/2_sx'; %directory used to create structure logfiles
logfiles = dir([di rn '/' '*.LOG']); %structure that contains characteristics of log files
for kf=1:length(logfiles) %reading each log file
    disp(['file #' int2str(kf) ' ' logfiles(kf).name]) %shows which log file is considered
    in iteration
    fname=logfiles(kf).name; %name of log file considered in iteration
    if kf==1 %do it only for first iteration
        eval(['cd ' di rn]) %go to directory where log files are
    end
    kk=1; %counter
    FC=readcell(fname); %creates cell array by reading from file "fname"
    for ii=1:length(FC) %considers each row of FC
        FCappo=[]; %auxiliar cell array
        for jj=1:length(FC{ii,:}) %considers each column of FC
            if max(size(FC{ii,jj}))>1
                FCappo=[FCappo ',' FC{ii,jj}];
            elseif and(max(size(FC{ii,jj}))==1, isfloat(FC{ii,jj}))
                FCappo=[FCappo ',' num2str(FC{ii,jj},15)];
            end
        end
    end

    % ANALYSE CELL ARRAY
    if isempty(FCappo)
        appo=false;
    else
        appo=contains(FCappo,'BESTPOSA');
    end

    if (appo==1)
        i1=strfind(FCappo,'NARROW_INT,'); %find where the coordinate string start
        i2=strfind(FCappo,'BESTPOSA'); %find where the time string start
        if (isempty(i1)||isempty(i2)) %check if there is no coordinate and time string
            continue
        end

        % TIME
        timeString=FCappo(i2:i1); %write the string that contain the time data
        i c1=find(timeString==','); %find the the index of comma that divide the data
        tempo(kk,1)=str2num(timeString(i c1(6)+1:i c1(7)-1)); %find the time data

        % COORDINATES
        coordinateString=FCappo(i1+11:i1+100); %write the string that contain the
        coordinate data
        i c2=find(coordinateString==','); %find the index of comma that divide the data
        lat(kk,1)=str2num(coordinateString(1:i c2(1)-1)); %find the latitude data
    end
end

```

## Report on the activities of the European project GISCAD-OV

```
lon(kk, 1)=str2num(coordinateString(i c2(1)+1: i c2(2)-1)); %find the longitude
data
    alt(kk, 1)=str2num(coordinateString(i c2(2)+1: i c2(3)-1)); %find the altitude data
    kk=kk+1; %increase counter
end
end

% SAVE DATA
save(fname(1: end-4), ' tempo', ' lat', ' lon', ' alt' )
varsc={' tempo', ' lat', ' lon', ' alt', ' FC' };
clear(varsc{:});
end
```

[Published with MATLAB® R2020b](#)

## 5.2 Script for geodetic coordinates conversion

```

function [t, lam, phi, h, x, y, z, xEast, yNorth, zUp, xLocal, yLocal, zLocal] = ...
    dataConverter(fname)
%The function applies a coordinates' transformation. It takes as input the
%name of a file (string) which contains the variables tempo, lat, lon and
%alt. Those variables are respectively the time, latitude, longitude and
%altitude acquired from a Novatel sensor. The function gives back as output
%the coordinates expressed in three different reference system, which are
%the ECEF (Earth Centred Earth Fixed reference system), the ENU (Eastn
%North Up reference system) and the LOCAL reference system. The first two
%can be found in literature, the third one is the local reference system
%applied to the structure that is being analysed. It is tangent to the
%structure as the ENU reference system. The only difference is that the
%local one is rotated around the vertical axis of an angle specified by the
%user.
%fname = string that specifies the name of the file
%t = time vector
%lam = latitude vector
%phi = longitude vector
%h = altitude vector
%x = x vector in ECEF
%y = y vector in ECEF
%z = z vector in ECEF
%xEast = East vector in ENU
%yNorth = North vector in ENU
%zUp = Up vector in ENU
%xLocal = x vector in LOCAL
%yLocal = y vector in LOCAL
%zLocal = z vector in LOCAL

load(fname, 't', 'lam', 'phi', 'h')

% geo2ecef
% changing coordinates from GEODETIC to ECEF
wgs84 = wgs84Ellipsoid;
L = length(t); %number of acquisitions
ECEF = zeros(L, 3); %matrix of ECEF coordinates
for ii=1:L %acquisitions
    [ECEF(ii, 1), ECEF(ii, 2), ECEF(ii, 3)] = ...
        geodetic2ecef(wgs84, lam(ii), phi(ii), h(ii));
end
x = ECEF(:, 1);
y = ECEF(:, 2);
z = ECEF(:, 3);

% ecef2enu
% changing coordinates from ECEF to ENU
LATO = mean(lam); %reference latitude in ENU plane
LONO = mean(phi); %reference longitude in ENU plane
HO = mean(h); %reference altitude in ENU plane
ENU = zeros(L, 3); %matrix of ENU coordinates
for ii=1:L

```

## Report on the activities of the European project GISCAD-OV

```
[ENU(ii, 1), ENU(ii, 2), ENU(ii, 3)] = ...
    ecef2enu(x(ii), y(ii), z(ii), LATO, LONO, HO, wgs84);
end
xEast = ENU(:, 1);
yNorth = ENU(:, 2);
zUp = ENU(:, 3);

% enu2local
% changing coordinates from ENU to LOCAL
alpha = -14;
alpha_radians = alpha * pi / 180;
LOCAL = zeros(L, 3);
for ii = 1:L
    LOCAL(ii, :) = [xEast(ii)*cos(alpha_radians) - ...
        yNorth(ii)*sin(alpha_radians) xEast(ii, 1)*sin(alpha_radians) + ...
        yNorth(ii)*cos(alpha_radians) zUp(ii)];
end
xLocal = LOCAL(:, 1);
yLocal = LOCAL(:, 2);
zLocal = LOCAL(:, 3);
```

[Published with MATLAB® R2020b](#)

### 5.3 Script for data filtering

```
function [y, B, A]=bandpassfilter(Fi, Ff, n, u, Fc)
%function [y, B, A]=bandpassfilter(Fi, Ff, n, u, Fc);
%y= segnale filtrato
%Fi frequenza iniziale del filtro passa banda
%Ff frequenza finale del filtro passabanda
%n ordine del filtro
%Fc frequenza di campionamento

freqi =Fi/(Fc/2);
freqf=Ff/(Fc/2);
[B, A]=butter(n, [freqi, freqf]);
y=filter(B, A, u);
```

*Published with MATLAB® R2020b*

## 6 Bibliography

1. Portland State Aerospace Society. Conversion of Geodetic coordinates to the Local Tangent Plane. Earth. 2007;01.
2. Coordinate Systems (Spatial Reference Systems) [Internet]. [cited 2021 Nov 16]. Available from:  
[https://docs.oracle.com/cd/A91202\\_01/901\\_doc/appdev.901/a88805/sdo\\_cs\\_c.htm](https://docs.oracle.com/cd/A91202_01/901_doc/appdev.901/a88805/sdo_cs_c.htm)
3. Ruffhead A, Whiting BM. Surveying Working Paper No 01 / 2020 Introduction to geodetic datum transformations and. 2020;(October).
4. Heiskanen Moritz 1967 Physical Geodesy : San Francisco W. H. Freeman and Company : Free Download, Borrow, and Streaming : Internet Archive [Internet]. [cited 2021 Nov 18]. Available from:  
<https://archive.org/details/HeiskanenMoritz1967PhysicalGeodesy/page/n191/mode/2up>
5. Wang Y, Huynh G, Williamson C. Integration of Google Maps/Earth with microscale meteorology models and data visualization. Comput Geosci [Internet]. 2013;61:23–31. Available from: <http://dx.doi.org/10.1016/j.cageo.2013.07.016>
6. Canciani M, Falcolini C, Saccone M, Spadafora G. FROM POINT CLOUDS TO ARCHITECTURAL MODELS: ALGORITHMS FOR SHAPE RECONSTRUCTION. Int Arch Photogramm Remote Sens Spat Inf Sci [Internet]. 2013 Feb 13 [cited 2021 Dec 7];XL-5/W1:27–34. Available from:  
[https://www.researchgate.net/publication/285720754\\_From\\_point\\_clouds\\_to\\_architectural\\_models\\_Algorithms\\_for\\_shape\\_reconstruction](https://www.researchgate.net/publication/285720754_From_point_clouds_to_architectural_models_Algorithms_for_shape_reconstruction)
7. NovAtel. Commands and Logs OEM7 Commands and Logs Reference Manual. 2017;(June).
8. All You Need to Know about the GPS / GNSS Week Number Rollover | Septentrio [Internet]. [cited 2021 Nov 25]. Available from:  
<https://www.septentrio.com/en/learn-more/insights/all-you-need-know-about-gps-gnss-week-number-rollover>

9. Welch PD. The Use of Fast Fourier Transform for the Estimation of Power Spectra: A Method Based on Time Averaging Over Short, Modified Periodograms. IEEE Trans Audio Electroacoust. 1967;15(2):70–3.
10. UTC to GPS Time Correction - Qinsy [Internet]. [cited 2021 Nov 26]. Available from: <https://confluence.qps.nl/qinsy/latest/en/utc-to-gps-time-correction-32245263.html>